

Energetic Particles from Quasi-Separatrix Layers and Current Sheets at the Sun

NATHAN A. SCHWADRON,¹ RONALD M. CAPLAN,² JON A. LINKER,² ERIKA PALMERIO,² AND MATTHEW A. YOUNG¹

¹*University of New Hampshire, Morse Hall, 8 College Road, Durham, NH, 03824, USA*

²*Predictive Science Inc., 9990 Mesa Rim Road, Suite 170, San Diego, CA, 92121, USA*

ABSTRACT

Quasi-separatrix layers (QSLs) at the Sun are created from regions where channels of open magnetic flux have footpoints near regions of large-scale closed magnetic flux. These regions are particularly prone to magnetic reconnection at the Sun. In recent simulations of coronal mass ejections (CMEs) with the Magnetohydrodynamic Algorithm outside a Sphere (MAS) model coupled to the Energetic Particle Radiation Environment Module (EPREM) model, common sources of energetic particles were discovered over broad longitudinal distributions in the background solar wind, far from the sites of particle acceleration driven by compressions and shocks in front of CMEs. Further investigation revealed these to be accelerated energetic particles from the QSLs and current sheets. The energy released from magnetic reconnection near the QSL drives reconnection exhausts and field-aligned flows, which in turn accelerate energetic particles. The reconnection process also releases material previously contained within closed magnetic field structures, which are often rich in heavy ions and ³He ions, as corroborated by recent PSP observations. Therefore, the seed populations produced by QSLs are expected to be rich in ³He and heavy ions. Thus, we present the first global model of energetic particles accelerated from QSLs and above current sheets from the Sun. Our results provide a plausible source for seed populations near the Sun, which likely have ³He and heavy ion enhancements. These results aid in the development of predictive solar energetic particle models.

1. INTRODUCTION

Solar energetic particles (SEPs) are high-energy, charged particles that are accelerated and transported in the solar corona and solar wind. Large fluxes of SEPs are present in solar particle events (SPEs), which represent a significant hazard for humans and technological infrastructure. SPEs can harm aircraft avionics, communications, and navigation systems. They also represent a possible risk to the health of airline crews and passengers on polar flights. In space, SPEs can be hazardous for crews of Low Earth Orbit spacecraft and the International Space Station, especially when engaged in extravehicular activity. They may also imperil crews of future manned lunar or interplanetary missions. Understanding the origin of SPEs and predicting the resulting fluxes at different locations in the heliosphere is therefore not only significant scientifically, but is also important from a space weather perspective.

SEPs are associated with solar eruptions; specifically solar flares and coronal mass ejections (CMEs, e.g., Reames 2013). Since the 1990s, SEPs have been roughly divided into impulsive events, associated with magnetic reconnection in short-duration solar flares, and gradual events, believed to be accelerated by shock waves driven by CMEs (Reames 1999). An important question for shock-accelerated SEPs in large gradual events is the source of the suprathermal seed population, which may be remnants of earlier flares/CMEs (Mewaldt et al. 2012). A more complex picture has emerged from recent observations (Anastasiadis et al. 2019, and references therein), with reconnection possibly playing a role in gradual events. In large solar eruptions, CMEs and flares are typically closely associated and are believed to be the result of the same underlying process that disrupts and reconfigures the coronal magnetic field (e.g., Forbes 2000). While the initiation mechanism(s) are still under debate, magnetic reconnection is seen to be an important part of the energy release process in CMEs (e.g., Green et al. 2018, and references therein).

Solar flares are thought to be fundamentally related to magnetic reconnection. In the standard model of flare reconnection, open magnetic field lines are swept through a current sheet, reconnecting with each other to form cusp-shaped loops in the corona. These cusp-shaped loops then relax into a more potential, rounded state (Priest & Forbes 2002). This is sometimes referred to as field line shrinkage (Švestka et al. 1987). One of the difficulties in this model for understanding SEPs is that the contraction of the field lines that leads to particle acceleration (Somov & Kosugi 1997; Tsuneta & Naito 1998) occurs on closed magnetic field lines. Therefore, the release of SEPs on open magnetic field lines requires either interchange magnetic reconnection between open magnetic field lines and the previously closed magnetic loops or cross field diffusion from the closed magnetic field lines onto open magnetic field lines. The outflow exhausts from any form of magnetic reconnection can be very fast, provided that the Alfvén speed in the outflow region is large. In the corona, Alfvén speeds are typically 500 km/s in weak field regions, but can become extremely large (10,000–20,000 km/s) where fields are strong. Shock waves will likely exist at the termination of the exhaust. Shock waves produced by impulsively-driven reconnection may be important during flares or during the emergence of magnetic flux from the photosphere into the corona. Forbes (1986), Blackman & Field (1994), and Workman et al. (2011) have investigated such shock waves by studying numerical experiments using 2D magnetohydrodynamics (MHD).

For particles accelerated by reconnection processes to be measured in interplanetary space, they must escape the the closed magnetic field region. Interchange reconnection between open and closed field lines is considered the most likely mechanism. This process was considered originally as a concept for the origin of slow solar wind. Axford (1977) and Fisk & Schwadron (2001) argued that the solar wind from the polar coronal holes should be substantially different from the solar wind from the low-latitude return region where open magnetic flux encounters and undergoes reconnection with closed coronal loops. The resulting solar wind should therefore be highly variable, as is observed, and presumably slow. This concept also offers an explanation for compositional differences between the fast and slow solar wind (Schwadron et al. 1999). The material stored in loops may, as a result of wave heating, contain enhancements in elements with low first ionization potential (FIP). Further, the loops may act as conduits for the solar wind by temporarily storing and heating plasma to higher coronal temperatures.

The reconnection process between open and closed magnetic flux causes intermittent changes in the footpoints of open magnetic field lines. After each reconnection between open and closed field lines, the open field footpoint hops from its previous location to the closed field footpoint that has a magnetic polarity matching that of the open magnetic field line.

Crooker et al. (2002) demonstrated that CMEs should also cause reconnection between closed and open magnetic flux. Until 1995, disconnection at the Sun was thought to be the only solution to the problem of balancing the magnetic flux of CMEs added to the heliosphere, in spite of the fact that the expected solar wind signature of disconnection was rare. Disconnection was pictured as merging between open field lines to create completely disconnected U-shaped structures or merging between closed field lines to create, in two dimensions, completely disconnected plasmoids. Since 1995, both theoretical and observational studies have made important contributions toward a revision of this solution. On the basis of a synthesis of these studies, Crooker et al. (2002) suggested that the primary flux balancing mechanism is not complete disconnection but rather merging between closed and open fields, i.e., interchange reconnection.

The closed CME magnetic flux undergoing interchange reconnection will move the reconnected open flux by at least the CME footpoint separation distance. Since the polarity of CME footpoints tends to follow a pattern similar to the Hale cycle of sunspot polarity, repeated CME eruption and subsequent reconnection will naturally result in latitudinal transport of open solar flux.

The topology in 3D magnetic configurations (Baum & Bratenahl 1980) is known to play a significant role in eruptive processes leading to solar flares and CMEs. Current sheets form naturally near thin separatrices where the magnetic field vanishes or becomes very weak (e.g., Aly 1990; Low & Wolfson 1988; Lau 1993). Magnetic reconnection along a separator changes the current system, often leading to the large release of energy stored within them (Henoux & Somov 1987). Observed solar flares show that the field lines closest to the separator connect to bright ribbons in the chromosphere (Somov et al. 1998), indicating the relationship between large current sheets and energy release from the magnetic field and plasma.

Quasi-separatrix layers (QSLs) are regions from the Sun in which magnetic fields have strongly varying field connectivity (Demoulin et al. 1996; Démoulin et al. 1996). They are configured in complex 3D topologies that are preferential locations for current sheet development and magnetic reconnection. Observed flares have been studied based on the QSL field connectivity down to the chromosphere (Demoulin et al. 1997; Mandrini et al. 1997; Bagalá et al. 2000).

MHD models of the solar corona (Antiochos et al. 2011; Linker et al. 2011; Titov et al. 2011) revealed that a web of separators and QSLs, primarily associated with the helmet streamer belt, should surround the Sun in the middle corona. This “S-web” was proposed as a natural location for interchange reconnection and a source for the slow solar wind. Interchange reconnection dynamics were subsequently demonstrated in MHD simulations (Higginson et al. 2017; Higginson & Lynch 2018), and observational evidence for the S-web as a dynamical slow solar wind source has recently been presented (Baker et al. 2023; Chitta et al. 2023).

In this paper we discuss recent results of MHD modeling and energetic particle acceleration modeling indicating that there are specialized sites above large-scale current sheets and QSLs, associated with the S-web, where energetic particle populations are accelerated. The results of modeling and analytical treatments developed within appendices suggest that QSL-associated particle acceleration naturally provides the seed population for energetic particles, and helps to broaden the longitudinal distribution of accelerated particles from CME-driven acceleration.

The paper is organized as follows: In §2 we summarize the models used for analysis, and results of global simulations. In §3, we discuss the signatures of energetic particle acceleration from QSLs, and the mechanisms responsible for the acceleration of particles from these regions. We also discuss particle escape from QSL acceleration regions (§3.3), the characteristics of seed populations from QSLs (§3.4), and the composition of these seed populations (§3.5). §4 concludes the paper, and summarizes our key findings.

Beyond the main text, a number of appendices are developed to provide analytic insights into the nature of the model solutions. Appendix A examines the nature of the QSL particle acceleration, and produces a transport equation that relates QSL acceleration to momentum diffusion. In Appendix B, we solve the equation in Appendix A for 2D acceleration regions. In Appendix C, we show how QSL acceleration is connected with random stochastic acceleration processes. The connection is then used to understand how QSL acceleration operates down to low energies near the core of the solar wind.

2. INTEGRATED MHD-FOCUSED TRANSPORT MODELING OF SOLAR PARTICLE EVENTS

To model SPEs, we employ the SPE Threat Assessment Tool (STAT; Linker et al. 2019). STAT couples MHD simulations of CME events from Predictive Science Inc.’s Corona Heliosphere (CORHEL) modeling suite with focused transport simulations of solar energetic particles (SEPs) from the University of New Hampshire’s Energetic Particle Radiation Environment Module (EPREM). STAT allows users to run EPREM for previously computed Magnetohydrodynamic Algorithm outside a Sphere (MAS) simulations of real CME events to simulate SEP events and provide diagnostics that can be compared with observations.

2.1. MAS Simulations

The properties of compressive regions such as shocks that drive SEP acceleration depend critically on the properties of the local plasma environment. To model a specific event, the simulation must realistically capture these properties for the time period under study. The MAS model has a long history of continued development and applications to this problem. While models with a simple energy equation can qualitatively reproduce coronal properties (Mikić & Linker 1996; Linker et al. 1999; Mikić et al. 1999) and are sufficient for exploring some dynamical aspects of boundary evolution (Linker et al. 2011), so-called thermodynamic MHD models (Lionello et al. 2009; Riley et al. 2011, 2012; Downs et al. 2013; Linker et al. 2017; Titov et al. 2017; Mikić et al. 2018) are necessary to compute the plasma density and temperature with sufficient accuracy to simulate extreme ultra-violet (EUV) and X-ray emission observed from space. In this approach, the energy equation accounts for anisotropic thermal conduction, radiative losses, and coronal heating. Inclusion of these extra physical terms is vital for obtaining realistic Alfvén speeds (V_A) and sound speeds (C_S).

To model a specific time period, a full-Sun map of the photospheric magnetic field is obtained from an observatory or flux transport model and processed to create a boundary condition for the radial magnetic field (e.g., Linker et al. 2017). For this event, we developed a thermodynamic MHD simulation of the global corona using the procedure and equations described by Lionello et al. (2009), but with a Wave-Turbulence-Driven (WTD) description of coronal heating (e.g., Mikić et al. 2018). In this thermodynamic model, the temperature at the lower boundary is set to 17,500 K, similar to the upper chromosphere, and the upper boundary is at $30 R_\odot$, beyond the sonic and Alfvén critical points.

The CORHEL-CME modeling suite (Linker et al. 2024) uses MAS to compute solutions in the coronal ($1\text{--}30 R_\odot$) and heliospheric ($28\text{--}230 R_\odot$) domains separately. Coronal solutions are used to provide the inner boundary condition

for the heliospheric solutions for both steady-state background and dynamic CME simulations (Lionello et al. 2013). In principle, MHD solutions for both the coronal and heliospheric domains can be included in the EPREM calculation (described in §2.2). At the present time, STAT employs only the MHD coronal domain within EPREM, and the remainder of the heliosphere is modeled with a simple spiral magnetic field created with a radially constant solar wind speed. This restricts us to modeling the first few hours of an SEP event; once the CME leaves the coronal portion of the domain, possible SEP acceleration from the CME propagation in the heliosphere is not modeled. STAT is presently being modified to incorporate both the coronal and heliospheric solutions in the EPREM simulations; these results will be the subject of future publications.

2.2. EPREM Focused Transport Simulations

EPREM models energetic particle acceleration and transport using a Lagrangian system, which co-moves with the plasma. EPREM creates a spherical shell of simulation nodes at each time step and advances each node according to $\Delta\vec{r} = \vec{V}\Delta t$, where \vec{r} is the 3D node displacement, \vec{V} is the 3D flow velocity (here, taken from the MAS simulation), and Δt is the time step duration. It then calculates the distribution function for species s , $f_s(t, r, p, \mu)$, according to the focused transport equation,

$$\begin{aligned}
 & \frac{df_s}{dt} && \text{(convection)} \\
 & + v\mu\hat{b} \cdot \nabla f_s && \text{(streaming)} \\
 & + \frac{(1-\mu^2)}{2} \left[-v\hat{b} \cdot \nabla \ln B - \frac{2}{v}\hat{b} \cdot \frac{d\vec{V}}{dt} + \mu \frac{d \ln(n^2/B^3)}{dt} \right] \frac{\partial f_s}{\partial \mu} && \text{(adiabatic focusing)} \\
 & + \left[-\frac{\mu}{v}\hat{b} \cdot \frac{d\vec{V}}{dt} + \mu^2 \frac{d \ln(n/B)}{dt} + \frac{(1-\mu^2)}{2} \frac{d \ln B}{dt} \right] \frac{\partial f_s}{\partial \ln p} && \text{(cooling)} \\
 & = \frac{\partial}{\partial \mu} \left(\frac{D_{\mu\mu}}{2} \frac{\partial f_s}{\partial \mu} \right), && \text{(pitch-angle scattering and injection)} \quad (1)
 \end{aligned}$$

where t is time, p is momentum, μ is the pitch-angle cosine, \hat{b} is a unit vector parallel to the magnetic field \vec{B} , v is the particle velocity (distinct from the flow velocity \vec{V}), and $D_{\mu\mu}$ is the pitch-angle diffusion tensor. EPREM uses a relaxation-time approximation for pitch-angle diffusion with the relaxation time inversely related to the pitch-angle diffusion coefficient. This treatment is applied for simplicity and significantly reduces computational cost.

Each node advances outward with the solar wind flow and is linked to nodes on the neighboring shells. Each linked sequence of nodes defines a simulation stream representing a velocity path line—the trajectory of fluid particles. In steady-state (i.e., in the frame rotating with the Sun) these are also streamlines; in places where the frozen-in assumption of ideal magnetohydrodynamics (MHD) holds, these lines also represent magnetic field lines.

The advantage of solving the transport problem in the co-moving frame is that it precludes the necessity of computing spatial gradients in flow velocity, which tend to introduce numerical errors (such as extraneous cross-field diffusivity) that accumulate over many time steps. Instead, it requires the relatively simple task of computing the rates of change in plasma number density, n , and \vec{B} at each stream node after being moved by a timestep. This methodology is based on the approach described in Kóta et al. (2005), which follows from the theory developed by Skilling (1971) and Ruffolo (1995). It was used by Kozarev et al. (2013) to study time dependent effects of SEP acceleration in the low corona during CME evolution and by Schwadron et al. (2014a) to model radiation doses at 1 au during a strong SPE event. In order to solve Equation 1, EPREM needs a model of n , \vec{B} , and \vec{V} at each node. Simplified scenarios can use analytic forms of these plasma quantities but realistic modeling requires the use of MHD data such as that provided by CORHEL-CME.

One recent study used EPREM and CORHEL to model the 2000 July 14 solar proton event (Young et al. 2021). This work highlighted use of the software suite within the STAT framework to model proton acceleration to GeV energies due to the passage of the CME through the low solar corona. The simulations were compared to GOES-8 observations. Simulation results roughly reproduced the peak event fluxes and the timing and spatial location of the energetic particle event. The model was found to accurately describe the acceleration processes in the low corona and resolved the sites of most rapid acceleration close to the Sun. Integral flux envelopes from multiple simulated observers

near Earth further improve the comparison to observations and increase potential for predicting SPEs. Broken power-law fits to fluence spectra agreed with diffusive acceleration theory over the low-energy range. Over the high-energy range, they demonstrate the variability in acceleration rate and mirror the inter-event variability observed in solar cycle 23 ground-level enhancements.

2.3. Modeled Event: November 29, 2020 CME

We show results of a modeled CME event that demonstrates the coupling between the MAS and EPREM simulations. Model results show broad longitudinal features, as is the subject of this paper.

The CME that occurred on November 29, 2020 in NOAA AR 12790 attracted considerable attention in the solar community (e.g., Kollhoff et al. 2021; Mitchell et al. 2021; Cohen et al. 2021; Kouloumvakos et al. 2022; Palmerio et al. 2022). At the time, it was associated with the largest flare (M4.4 class) in three years and produced a shortwave radio blackout over the South Atlantic. In fact, the flare was likely even larger, given that its emission was partially occulted by the solar limb. This event is of particular interest here because it was the apparent source of the first broad longitude SEP event of cycle 25, with particle fluxes measured at Parker Solar Probe (PSP), at Solar Orbiter, at STEREO-A, near Earth, and at Mars. The mechanisms that create broad longitude SEP events are a topic of active research (e.g., Dresing et al. 2012; Lario et al. 2016), and several widespread events have been already observed and studied over solar cycle 25 after the November 29, 2020 one (e.g., Dresing et al. 2023; Khoo et al. 2024). These events are important from a space weather perspective. For example, unexpectedly fast rise times of SEPs far from the apparent source could be dangerous for astronauts and make it difficult to provide reliable forecasts of all-clear times.

Modeling the CME event is a complex task that involves several steps (e.g., Török et al. 2018). First, we examine EUV images to identify the salient features of the event. Since this eruption took place just behind the solar limb as seen from Earth, we use a combination of SDO/AIA and STEREO/EUVI data for this task. Next, we produce a full-Sun magnetic map to create the boundary conditions for the magnetic field. The map used here is a blend of high-resolution SDO/HMI vector magnetic field data of the active region and a lower-resolution combination of synoptic maps that we previously used for our prediction of the December 14, 2020 eclipse¹. We then produce a thermodynamic MHD model for the global corona to build a relaxed, steady-state model of the corona and solar wind out to $30 R_{\odot}$.

Next, we construct a set of pre-eruptive flux-rope configurations using our interactive web interface, which employs the Regularized Biot–Savart Law (RBSL; Titov et al. 2018) model. To investigate the eruptive behavior of these configurations, we employ the $\beta = 0$ MHD approximation and compare CME properties such as the rise direction and morphology with coronagraph observations from STEREO/COR and SOHO/LASCO. After such a preliminary examination, we can produce a final simulation by inserting a pre-relaxed (stable) flux rope into the thermodynamic solution, and trigger an eruption by setting the rope’s axial current above the stable-equilibrium value. The flux-rope current can be adjusted (within reasonable limits) to match the observed CME speed. Figure 1 shows a few snapshots from our “final” thermodynamic MHD simulation of the November 29 CME. In this case, we set the initial flux-rope current to about 25% above the equilibrium value.

Results of the EPREM simulation are shown in Figure 2, which include the energetic particle signatures and acceleration from the front of the CME. In addition, fluxes are distributed longitudinally over an enormous region outside the CME front. To investigate the source of the longitudinal spread in energetic particles, we traced the location of the EPREM streams producing particle fluxes at 1 au back to their origin in the low corona. We found that the source locations lie along separators, including the heliospheric current sheet (HCS). These regions are most easily identified by plotting the squashing factor Q (the so-called S-web). It appears that the initial MHD wave that propagates around the Sun (see Figure 1) does not itself cause significant SEP acceleration, but the wave interacts with the S-web, causing localized reconnection. The flows and reconnection exhausts locally accelerate SEPs in the simulation. Figure 2 shows snapshots after the start of the eruption. In Figure 2, the panels at 0.23 hr and 0.62 hr show the imprints of the CME bubble punching through the S-web at longitudes $\sim 190^{\circ}$ – 310° . These are the legs of the flux rope; at this point the CME front is a few R_{\odot} above the solar surface. Below $2 R_{\odot}$ compressive flows are generated along the HCS and at S-web arcs. In Figure 2 at longitudes $< 190^{\circ}$ and $> 310^{\circ}$, and late in the evolution, we observe SEP fluxes generated over a wide range of longitudes.

¹ See <https://www.predsci.com/corona/dec2020eclipse/home.php>

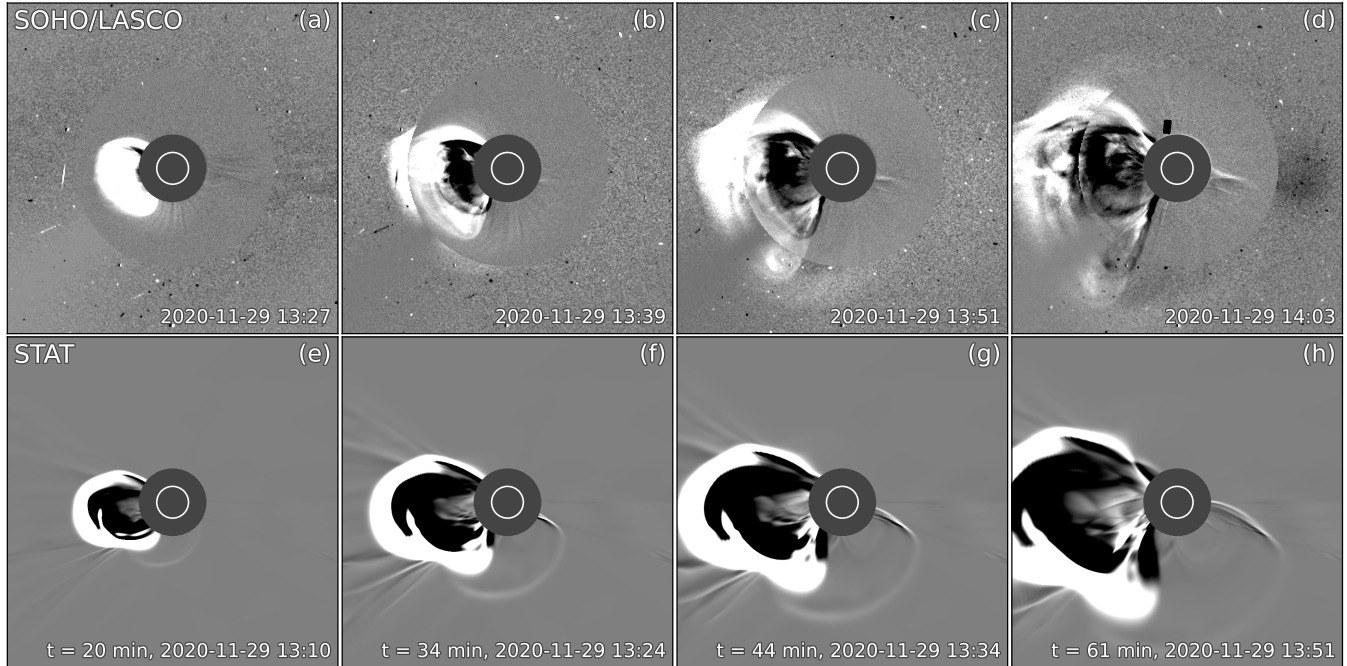


Figure 1. Comparison of the simulated CME and associated wave with LASCOCO white-light observations. (Top panels, a–d) Combined LASCOCO/C2+C3 running-difference brightness observations showing the CME and an associated wave at three times on 11/29/2020: 13:27, 13:39, 13:51, and 14:03 UT. (Bottom panels, e–h) Running difference of simulated brightness from the MHD simulation of the CME and its propagation. The time in minutes from the start of the simulated eruption is shown. The simulated CME and wave display qualitative similarities with the observed event, although there are differences in the morphology of the CME and timing of the wave.

Figure 3 (top right panel) shows the energetic particle fluxes more than 6 hr after the CME’s initial launch and propagation. At this point in time, the compressions caused by the CME’s acceleration have mostly moved out of the corona and into the inner heliosphere, but significant energetic particle fluxes remain relatively close to the Sun (near $2 R_{\odot}$) and the distribution of these fluxes strongly resembles the QSL pattern observed in the Figure’s bottom panels. The overlays in the bottom rows of Figures 2 and 3 make the explicit association between the QSL boundaries and energetic particle fluxes. The regions of enhanced energetic particle fluxes partly follow the outline of the HCS, but there are significant areas (such as 20° latitude, 270° longitude) where the energetic particle enhancements follow the QSL boundary even outside the current sheet. Conversely, there is not a one-to-one association between regions of high Q and elevated energetic particle fluxes. We show here in §3 that the particle acceleration is most significant in regions with strong and relatively localized reductions in the magnetic field, which accompany the exhausts from magnetic reconnection. Surprisingly, the enhanced energetic particle fluxes do not exclusively exist in regions of strong flow compression. The vast majority of QSL and current sheet regions studied outside the CME’s compression front show that the acceleration develops in response to the field reductions *in the absence of strong flow compression*.

We have also simulated the magnetic field and outflowing plasma in the absence of the November 29, 2020 CME. This simulation, referred to as the “Relaxation Run,” was also coupled with EPREM to study energetic particle fluxes in the relaxed field and flow configuration. The results of the Relaxation Run (left panels of Figure 3) are very similar to the late evolution (>6 hr) of the CME run (right panels of Figure 3), showing conclusively that energetic particles are accelerated near QSLs and current boundaries over broad longitudinal regions with or without an emitted CME.

3. QUASI-SEPARATRIX LAYER OUTFLOWS

In this section, we examine the MHD conditions near QSLs to characterize the outflows (§3.1). We use that characterization to understand whether the outflows have characteristics sufficient to generate the spectra observed in the seed population (§3.2). Particle escape from the QSL acceleration regions is considered in §3.3. We discuss the broader connection of QSL reconnection exhausts with stochastic processes and energetic particle seed populations in §3.4. Lastly, we discuss the chemical composition of seed populations from the QSL acceleration regions in §3.5.

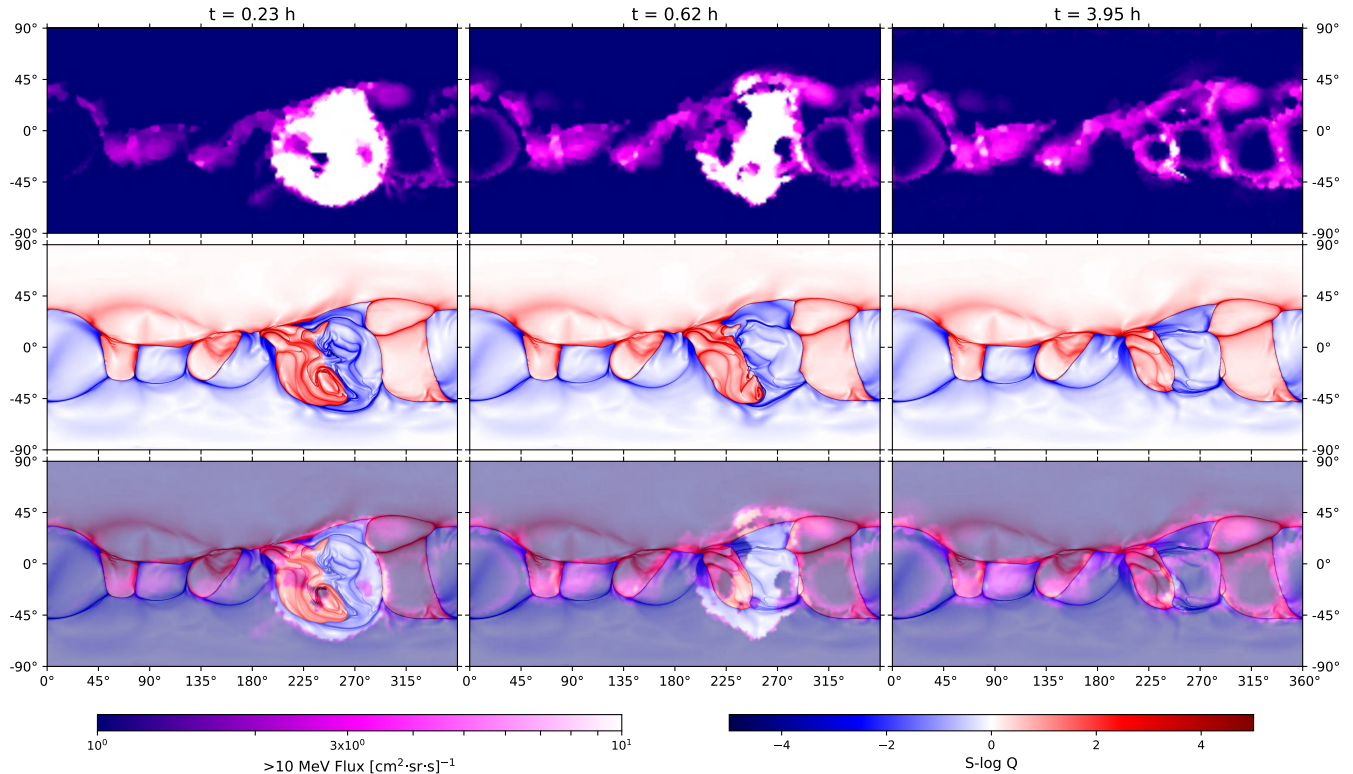


Figure 2. Distribution of energetic particle fluxes at $2 R_{\odot}$ from the 11/29/2020 event at three times from the start of the M class flare: +14 min, +37 min, and +3.95 hr. The energetic particle flux distributions show a strong enhancement where the CME moves out through the corona and solar wind. The top row of panels indicates the $>10\text{MeV}$ integrated fluxes computed by EPREM during the event. The middle row of images shows the log of squashing factor Q associated with QSLs (the S-web) with the red and blue coloring indicating the opposing polarity of the coronal magnetic field—data are displayed in *signed log* Q format, defined as $S\text{-log } Q \equiv \text{sign}(B_r) \log[Q/2 + (Q^2/4 - 1)^{1/2}]$ (Titov et al. 2011). The bottom row overlays these images to show the similarity between the spatial structures recovered.

3.1. QSL characterization

The question arises from §2.3 as to why we observe particle acceleration arising from QSL and current sheet boundaries. We ran the background solar wind configuration used for the November 29, 2020 event without a CME (left panels of Figure 3). The results showed enhanced energetic particle fluxes from the same regions of enhanced flux observed in Figure 2. Figure 4 shows the energetic particles ~ 4 hr after the simulation began. We highlight three specific streamlines: 1910, 3373, and 3105. Acceleration is observed at streamlines 1910 and 3373: streamline 1910 maps back to a QSL boundary without the current sheet boundary, and streamline 3373 maps back to a current sheet boundary. In contrast, streamline 3105, which is in a region without a QSL or current sheet boundary, does not show elevated fluxes relative to the seed spectrum. We observe elevated fluxes on a large fraction of the nodes that map to QSL boundaries, as observed during the November 29, 2020 CME event. However, with steady solar wind and no CME, we ask why elevated fluxes of energetic particles should be observed. In the next subsection (§3.2) we detail our examination of MHD quantities to determine the source of particle acceleration near QSLs and HCS boundaries.

3.2. Effects of QSLs on Energetic Particles

Figures 5–8 show the the rate of change for quantities that drive acceleration in Equation 1 along specific streamlines. The convective derivative of a given MHD quantity is evaluated by differencing values between points in time along the node history. For example, the convective derivative of the MHD density n is

$$\frac{1}{n} \frac{dn}{dt} = \frac{1}{n} \frac{\partial n}{\partial t} + \frac{\mathbf{u}}{n} \cdot \nabla n = -\nabla \cdot \mathbf{u}. \quad (2)$$

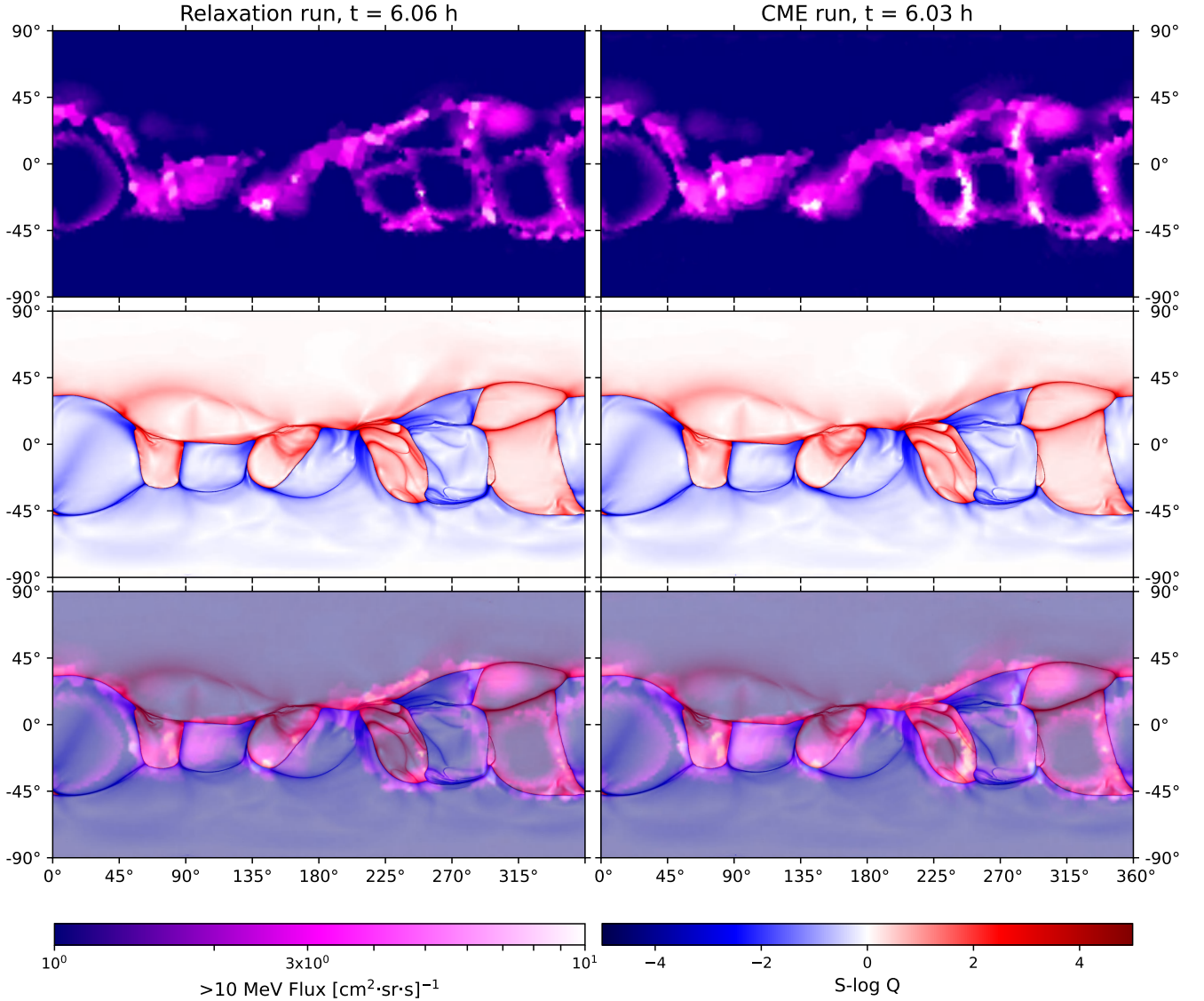


Figure 3. (Right panels) Energetic particle fluxes at $2 R_{\odot}$ from more than 6 hours after CME launch shown together with the QSL squashing factor to show consistency between energetic particle fluxes and the regions where strong QSL gradients drive more frequent magnetic reconnection. (Left panels) Energetic particle fluxes at $2 R_{\odot}$ over the same time period but with only background solar wind and magnetic fields (Relaxation Run). As in the right panels, we show the fluxes together with the QSL squashing factor.

This convective derivative at a given time ($t_{N+1/2}$) is found by differencing the density between the time-steps (t_N to t_{N+1}) that provide the nearest bounding neighbors in time along the node history.

The effects of the rates of change that drive particle acceleration are evaluated based on the results in Appendix A using the Focused Transport equation (see Equation A2). There are two significant particle acceleration terms in the Focused Transport equation:

$$\left[\frac{1}{3} \frac{d \ln n}{dt} \right] \frac{\partial f}{\partial \ln p}, \quad \text{and} \quad \left[\frac{(1 - 3\mu^2)}{2} \frac{d \ln(B/n^{2/3})}{dt} \right] \frac{\partial f}{\partial \ln p}. \quad (3)$$

The first term is associated with compression at shocks or compression regions, and the second term is associated with a combination of changes in magnetic flux density and density ($d \ln(B/n^{2/3})/dt$).

In Appendix A, we perform an expansion of the distribution with Legendre Polynomials, retaining the first three coefficients in the expansion. The approximation made is that pitch-angle diffusion drives the distribution toward

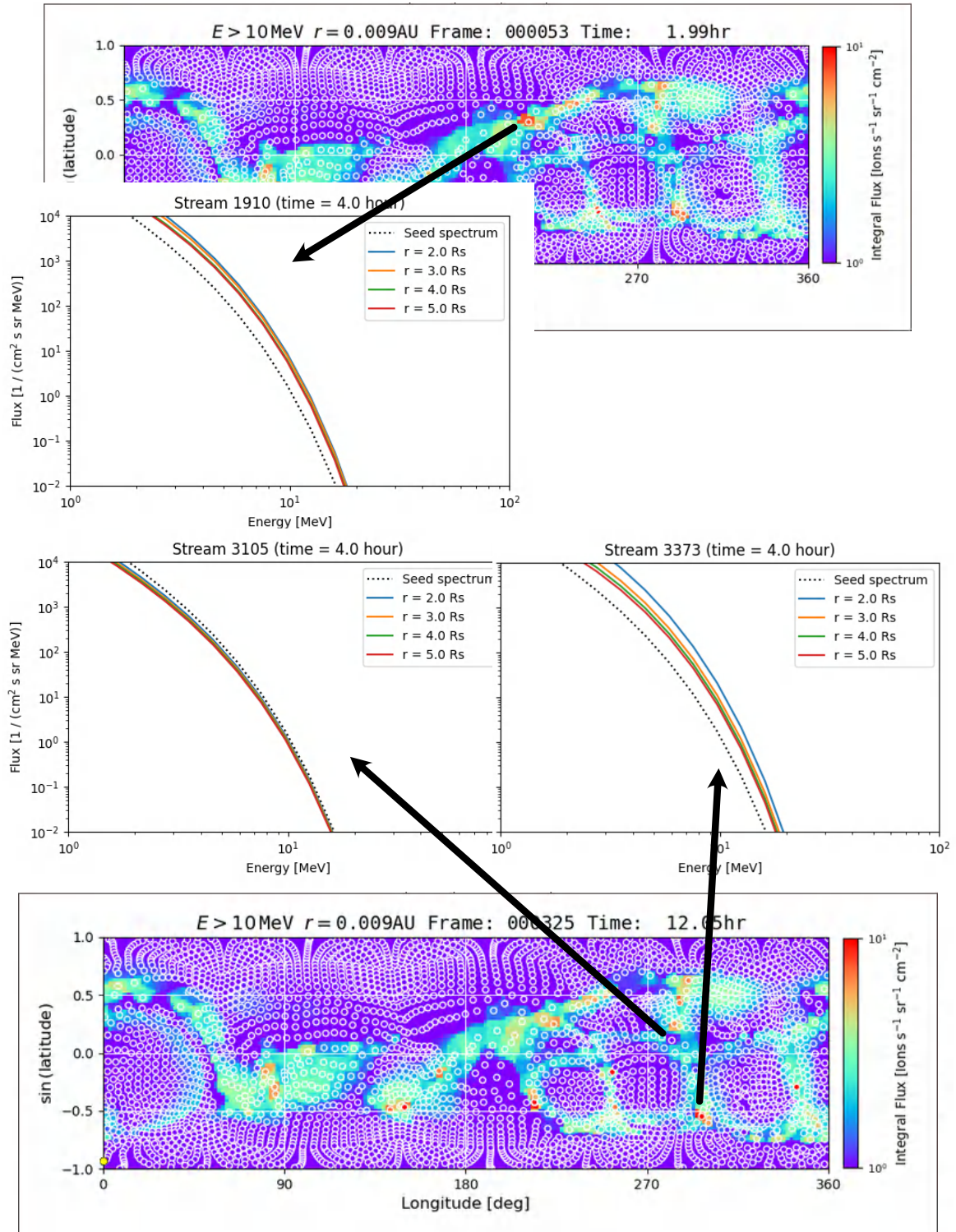


Figure 4. Differential fluxes of energetic particles at $2 R_{\odot}$ 4 hr into the simulation period with no CME. The simulation includes the background solar wind configuration used from the November 29, 2020 event. At the top and the bottom of the figure we show the node locations at $\sim 2 R_{\odot}$. The three cutouts show the energetic particle differential fluxes as a function of energy from three streamlines labeled 1910, 3373 and 3105. Significant acceleration is observed at streamlines 1910 and 3373, which map back to a QSL boundary and a current sheet boundary, respectively. In contrast, streamline 3105 does not show elevated fluxes relative to the seed spectrum and does not exist near a QSL boundary.

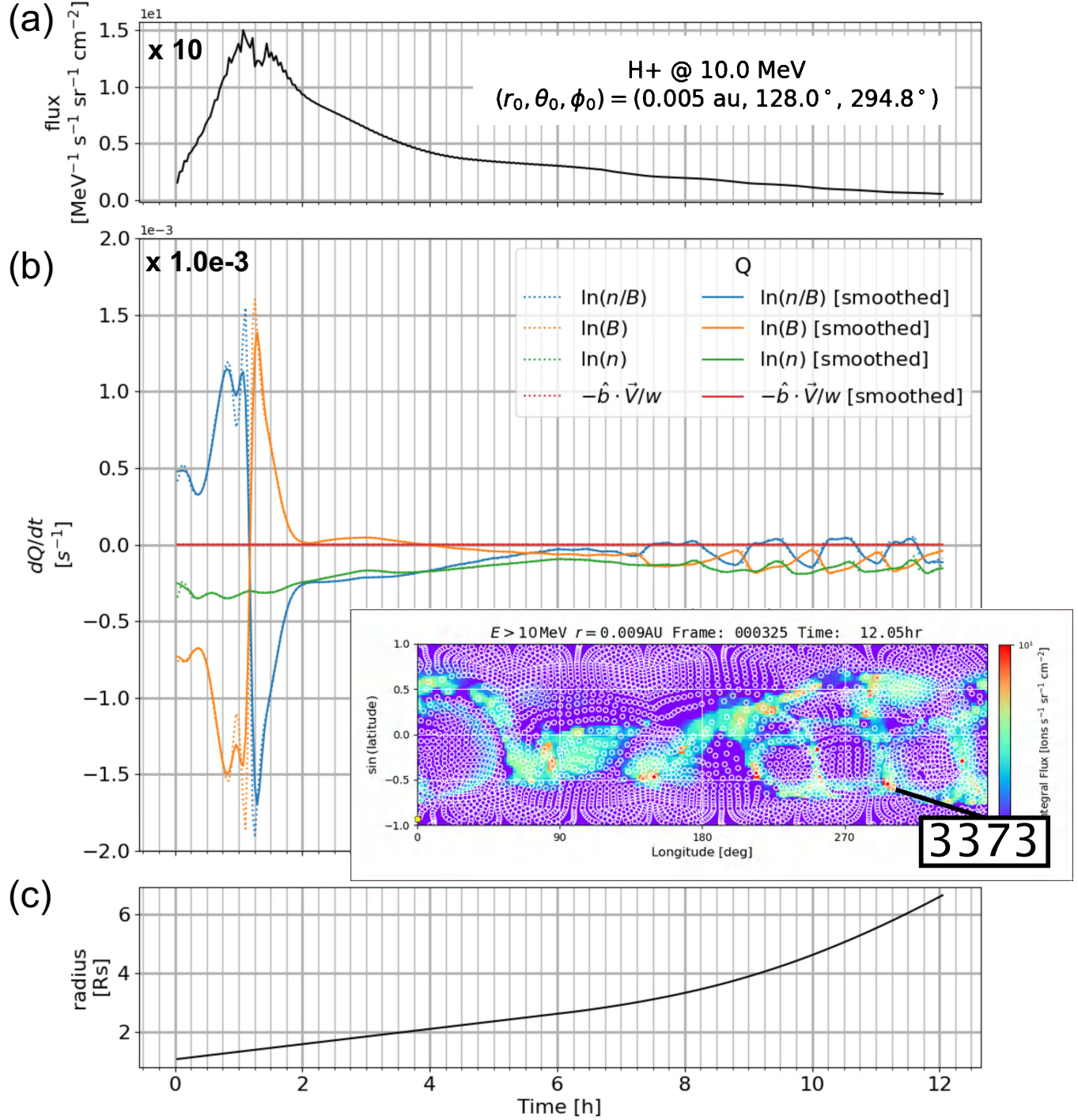


Figure 5. The rate of change for quantities that drive acceleration in Equation 1 (panel b), the differential flux at 10 MeV/nuc (panel a), and the radial distance from the Sun (panel c) of a node along streamline 3373. The dominant term driving acceleration is the rate of change of the magnetic field flux. As the node moves out approximately 0.4–2 hr into the simulation and traverses a region ~ 1.5 – $1.8 R_\odot$, we observe a large reduction and then a increase in the field strength associated with magnetic reconnection near the QSL boundary. The outflows of magnetic reconnection create an isolated region of rapid particle acceleration. We observe passage of the node through a reconnection outflow from a current sheet boundary.

isotropy. Retaining the first three moments of the distribution function is equivalent to a third-order expansion. This

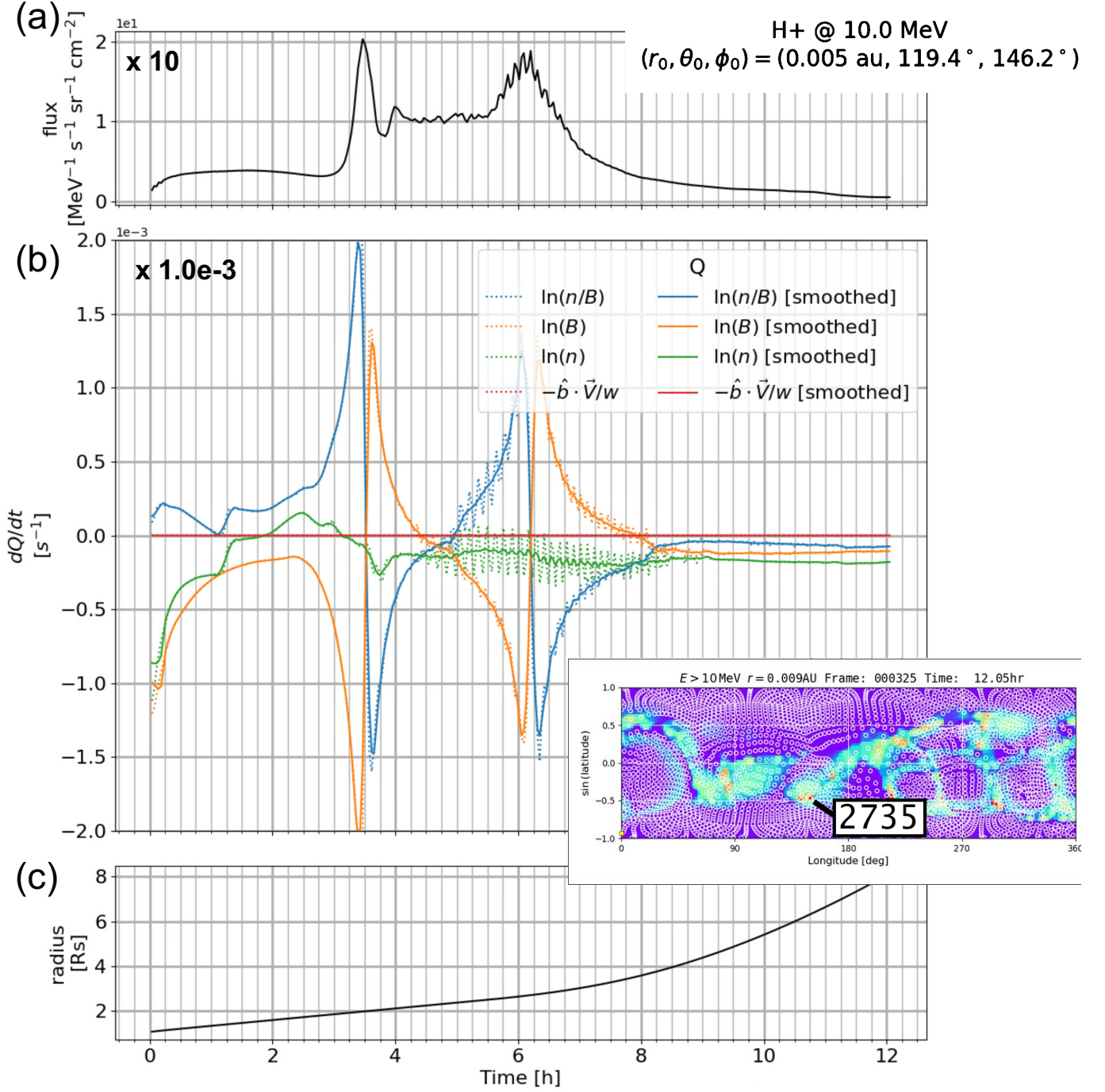


Figure 6. The rate of change for quantities that drive acceleration in Equation 1 in a format similar to Figure 5 for streamline 2735. We observe passage of the node through multiple reconnection outflows from the HCS boundaries.

approach has become standard for deriving the Parker equation and higher-order expansions that capture shear-related quantities in addition to compression (Williams et al. 1993). The expansion results in the following transport equation,

$$\frac{df_0}{dt} - \nabla \cdot (\bar{\kappa} \cdot \nabla f_0) - \frac{\nabla \cdot \mathbf{u}}{3} \frac{\partial f_0}{\partial \ln p} - \frac{1}{p^2} \frac{\partial}{\partial p} \left(p^2 D_{pp} \frac{\partial f_0}{\partial p} \right) = 0, \quad (4)$$

where

$$\bar{\kappa} = \frac{\lambda_{\parallel} v}{3} \hat{e}_b \hat{e}_b \quad (5)$$

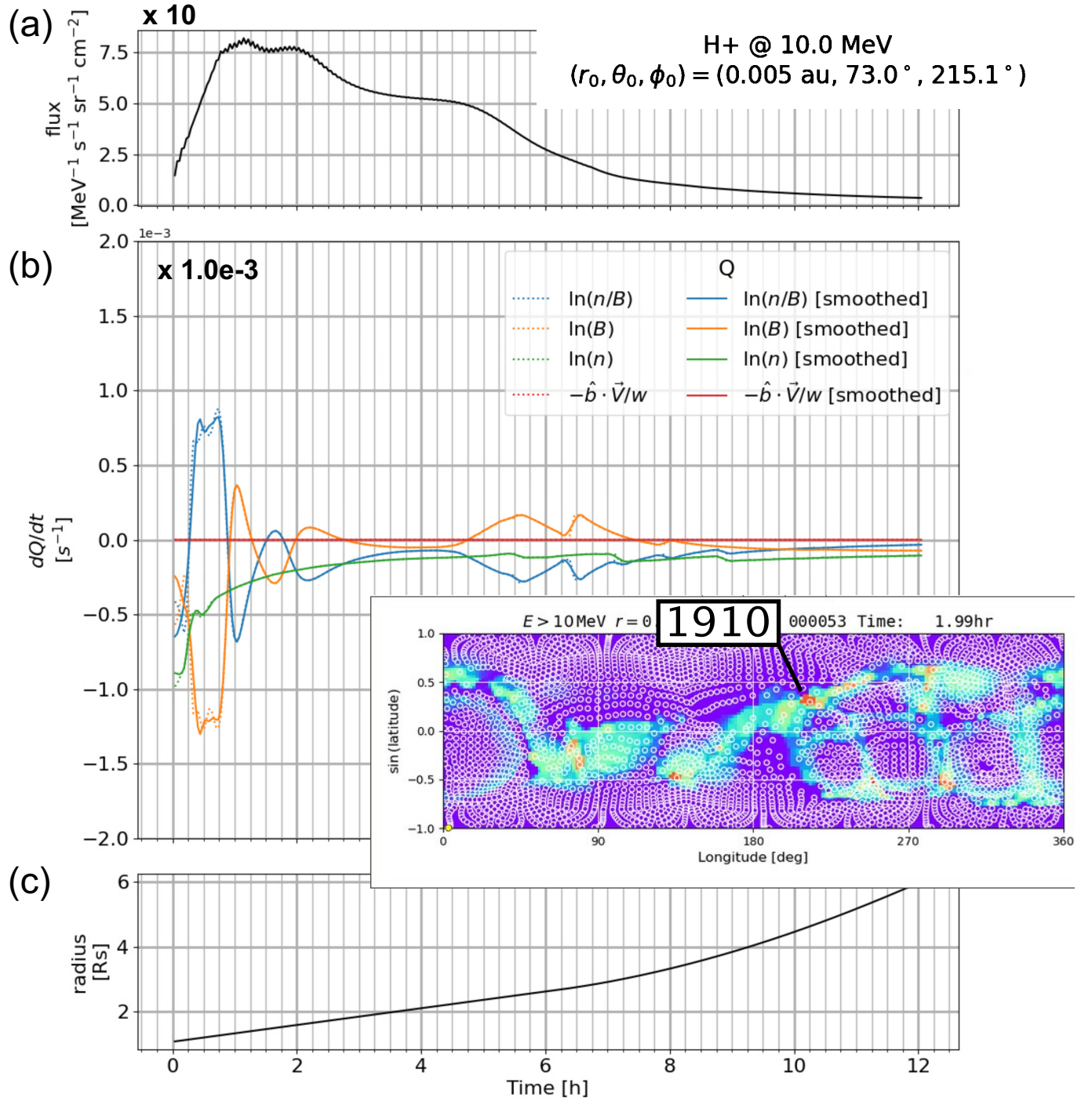


Figure 7. The rate of change for quantities that drive acceleration in Equation 1 in a format similar to Figures 5 and 6 for streamline 1910. The streamline passes through a reconnection outflow from a QSL boundary.

and

$$\frac{D_{pp}}{p^2} = \frac{\tau_s}{15} \left(\frac{d \ln(B/n^{2/3})}{dt} \right)^2. \quad (6)$$

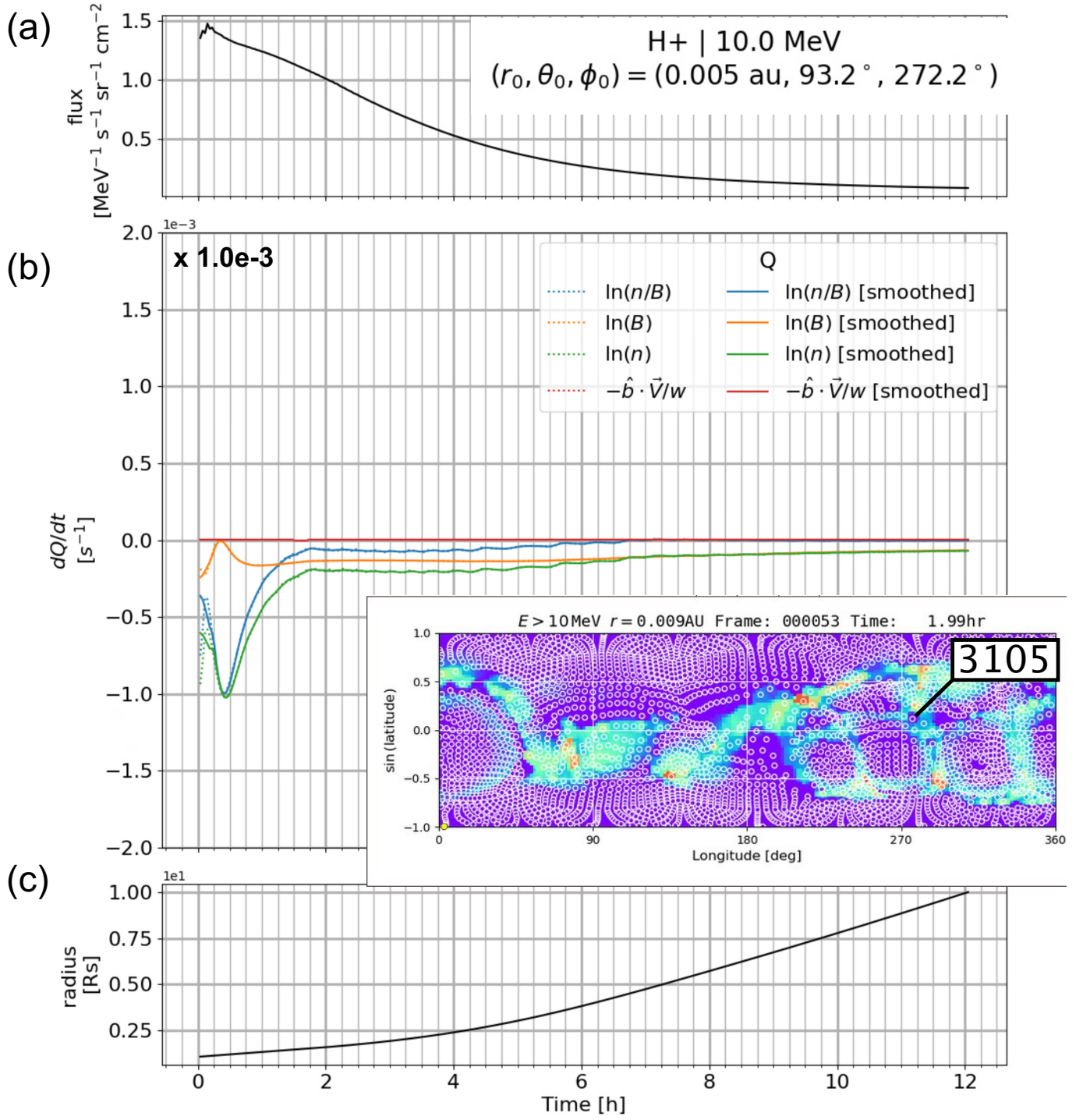


Figure 8. The rate of change for quantities that drive acceleration in Equation 1 in a format similar to Figures 5 and 6 for streamline 3105. The stream does not pass through a QSL node.

Here, f_0 is the isotropic part of the distribution function, and $\lambda_{\parallel} = \tau_s v$ is the scattering mean-free path. The result in Equation 4 is similar to the Parker transport equation, and includes a second-order diffusive acceleration term,

$$-\frac{1}{p^2} \frac{\partial}{\partial p} \left(p^2 D_{pp} \frac{\partial f_0}{\partial p} \right) \quad (7)$$

where the diffusive acceleration rate $D_{pp}/p^2 \propto \tau_s [d \ln(B/n^{2/3})/dt]^2$. Unlike diffusive shock acceleration, this second-order acceleration term occurs wherever there are strong gradients in the quantity $B/n^{2/3}$. While the momentum diffusion term increases with the scattering time τ_s , the diffusion rate cannot grow indefinitely since the scattering time must be sufficiently small to drive the distribution function toward the isotropy. In the limit of very large scattering times, the diffusion in momentum space is suppressed as particles propagate through the reconnection region, experiencing only local adiabatic changes in momentum and pitch-angle in response to changes in the field strength. Pitch-angle scattering is a critical component of the diffusive process.

Figures 5, 6, and 7 reveal that the dominant particle acceleration occurs where we observe a strong gradient in the magnetic field strength that is *not* accompanied by a strong expansion or compression in the density. In fact, as a node travels into the acceleration region, it first experiences a strong reduction in the magnetic field flux followed by an equivalent enhancement in the field flux. These regions occur naturally where magnetic reconnection exhausts create reductions in the magnetic field magnitude, as illustrated in Figure 9.

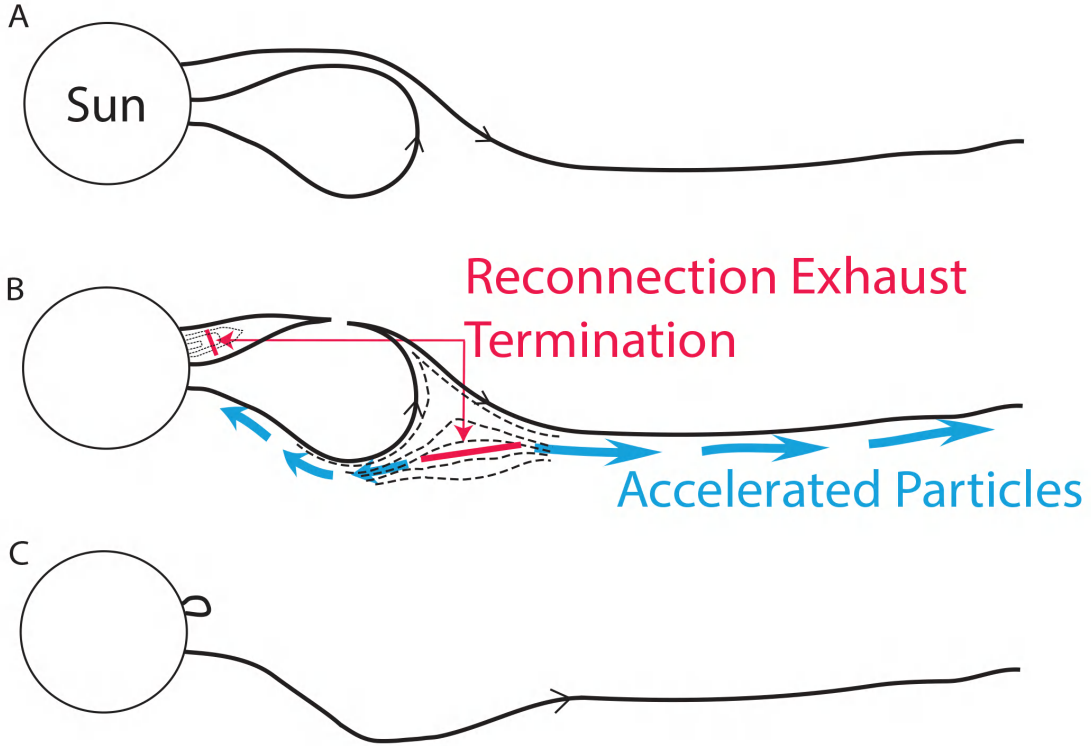


Figure 9. Schematic diagram of interchange reconnection and acceleration of energetic particles near the reconnection exhaust termination. An open magnetic field and a closed magnetic field line approach one another (Panel A). The simple closed topology shown here may actually be more complex, as discussed by Gosling et al. (1995). If the closed and open magnetic flux reconnect (Panel B), there are two outflow exhausts from the reconnection site. One exhaust is directed into the closed field region and the other exhaust is directed into the open field. The energetic particles accelerated within the exhaust that forms on the open magnetic field line (the lower side of panel B) are free to move throughout the inner heliosphere, and may provide seed populations for particles accelerated at the bow shocks of coronal mass ejections. Panel C shows the reconfiguration of the open and closed magnetic flux away from the reconnection exhaust.

Appendix B solves the transport equation (Equation B14) including both escape and diffusive acceleration at shocks or compressions. The rates of diffusion are characterized based on the dimensionless quantity LD_0/u defined as

$$\frac{LD_0}{u} = \frac{\tau_s L}{15 u} \left(\frac{d \ln(B/n^{2/3})}{dt} \right)^2 = D \left(\frac{p}{p_{\text{inject}}} \right)^\alpha, \quad (8)$$

where L is the characteristic size of the diffusive acceleration region, u is the wind speed through the reconnection exhaust. The quantity p_{inject} represents the injection momentum, α provides the scaling with particle momentum, and D is a dimensionless quantity for the amplitude of momentum diffusion. Similarly, the compression or shock is characterized by the relative change in plasma flow velocity, $\Delta u/u$, across the shock or compression. Results of solutions indicate that strong diffusion yielding a common characteristic spectrum with differential energy flux $j \propto E^{-1.5}$ occurs in the regime where $LD_0/u > 0.07$, whereas diffusion rates $LD_0/u < 0.005$ yield very soft spectra with energy power-laws typically softer than E^{-8} .

In Figure 10 we show the regimes of diffusive acceleration as a function of the scattering time τ_s multiplied by the acceleration region scale-size L , and divided by the wind speed u through the acceleration region. This quantity, $\tau_s \cdot L/u$, organizes the regimes of diffusive acceleration based on the rates of change $d \ln(B/n^{2/3})/dt$ within the reconnection exhaust.

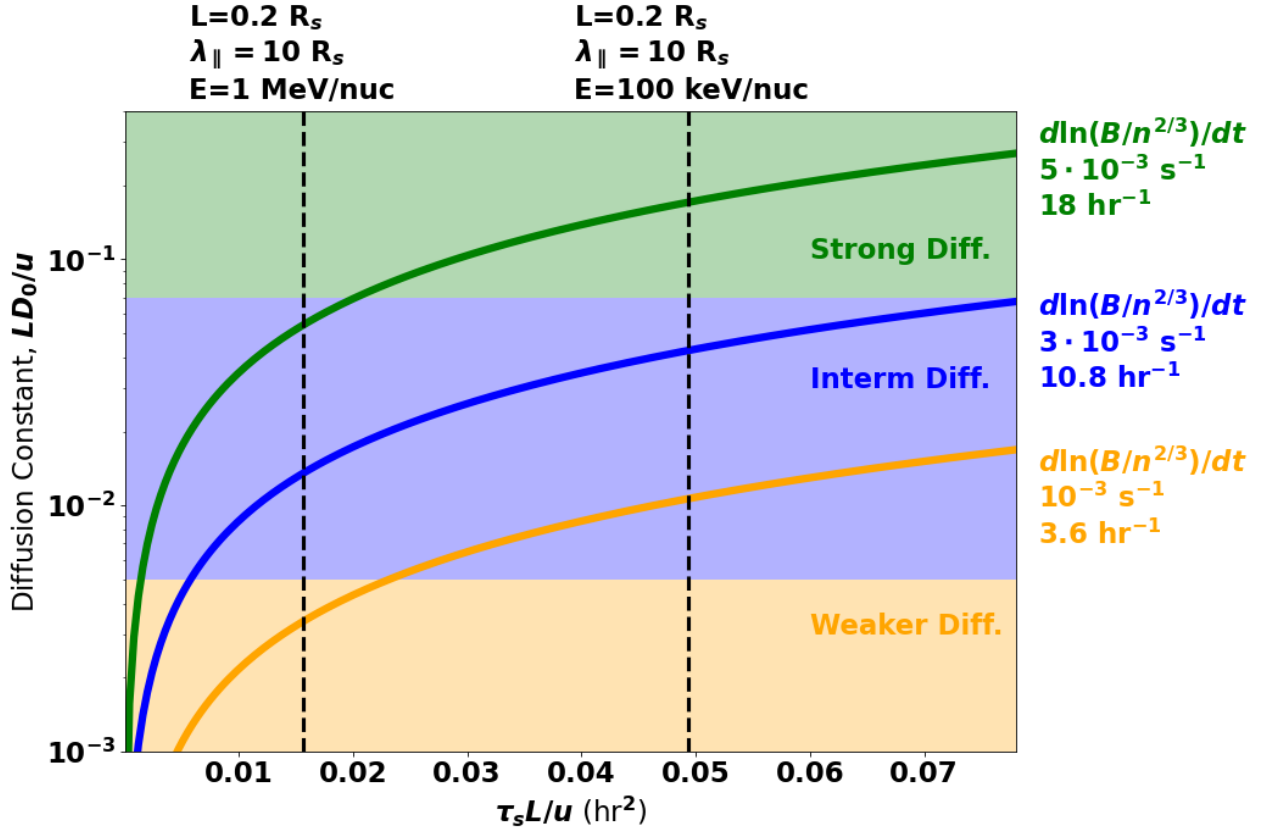


Figure 10. Regimes of diffusive acceleration based on the rates of change $d \ln B/n^{2/3}/dt$ associated with gradients in the reconnection exhaust. We show curves for the diffusion constant as a function of the scattering time τ_s multiplied by the acceleration region scale-size L , and divided by the wind speed u through the acceleration region. Three different curves are shown for the rates of change $d \ln B/n^{2/3}/dt$ associated with gradients in the reconnection exhaust. Gradients $d \ln B/n^{2/3}/dt > 2 \times 10^{-3} \text{ s}^{-1}$ result in intermediate to large diffusion constants, and for $d \ln B/n^{2/3}/dt > 3 \times 10^{-3}$, we observe diffusive acceleration rates sufficiently large to yield hard energy spectra approaching a common characteristic spectrum with differential energy flux $j \propto E^{-1.5}$ (see Figure 13).

The investigation of MHD terms causing particle acceleration highlights a surprising result. The compression (see green curves) from the reconnection regions is relatively small compared to the large reductions in magnetic field strength (orange curves) at both current sheet (Figures 5 and 6) and QSL boundaries (Figure 7). Large reductions in field strength without comparable changes in the density implies that magnetic flux tubes increase their area near the sites of reconnection, and the flow speed slows.

The particle acceleration near these sites is found to be driven by a second-order process, and is similar to particle acceleration caused by transit-time damping of fluctuations of magnetic field magnitude (Schwadron et al. 1996).

Unlike the first-order acceleration in shocks or compressions, there is no significant energy change for a particle that simply moves into and exits the reconnection region without scattering. However, an ion that is focused as it enters the reconnection region, and then scattered to larger pitch-angle while traversing the reconnection region, will experience a net energy gain upon its exit. After many encounters of the reconnection region, ions diffuse in momentum space, causing the build-up of suprathermal and energetic particle tails on the distribution functions.

3.3. *Escape from QSL acceleration regions*

Escape modifies the energy distributions associated with particle acceleration at shocks. Typically, escape is associated with an exponential high-energy roll-over or a broken power-law distribution. For example, in Schwadron et al. (2015), diffusive shock acceleration is used to model energetic particles formed from shocks or compressions low in the corona. Because these structures form close to the Sun, the regions of strong compression are typically on the fronts of the accelerating CME, or on the CME flanks where the rate of expansion close to the Sun is comparable to or faster than other forms of CME acceleration. In the low corona, there is large variability in the magnetic field's curvature and magnitude gradients, which causes significant variation in the compression along the CME front and flanks. The magnetic field connection along the shock or front changes rapidly, particularly in quasi-perpendicular structures, which are typical for the highly draped field configurations that form on fast CMEs associated with large SEP events. In these configurations, particles are swept along the compression by the magnetic field and eventually move off of the accelerating structure, and thereby escape rapid particle acceleration.

The QSL geometry is different than that of the strong field draping on the fronts of CMEs. In particular, we expect the exhaust region to form in a quasi-parallel field configuration. However, the lateral extent of exhaust is limited in scale. In this case, particle escape from acceleration regions is likely associated with cross-field diffusion. While the magnetic field itself remains in the reconnection exhaust, particles themselves move across magnetic field lines to exit the reconnection exhaust.

In Appendix B.3, we treat escape from the QSL region of characteristic size L . The escape energy is

$$E_{\text{esc}} = (3L/\lambda_{\perp})^2 E_{\text{sw}}, \quad (9)$$

where L is the scale-length associated with the QSL, and λ_{\perp} is the perpendicular diffusion mean free path. The energy $E_{\text{sw}} = mu_{\text{sw}}^2/2$ is the characteristic solar wind energy for a species of mass m in the upstream plasma (with speed u_{sw}). The escape process is discussed in Appendix B.3 where we take a parallel mean free path in the QSL region of $\lambda_{\parallel} = 5 R_{\odot}$, a characteristic QSL size of $L = 0.3 R_{\odot}$, and a ratio of perpendicular to parallel diffusion, $\eta = \lambda_{\perp}/\lambda_{\parallel} = 0.01$, leading to an escape energy $E_{\text{esc}} = 0.27$ MeV/nuc.

The EPREM simulations in this paper have not included cross-field diffusion explicitly. Therefore, the theoretical break imposed by escape will modify the spectra relative to those simulated. However, the EPREM simulations do include a seed spectrum with an energy roll-over near 1 MeV/nuc. In some sense, this roll-over mimicks the escape of energetic particles from the QSL.

3.4. *Seed Population Fluxes from the QSL region*

Appendix B.2 provides an analytic solution for particle acceleration within the large-scale QSL. Within the QSL, magnetic reconnection occurs frequently between closed magnetic structures and the open field lines that guide the solar wind. Particle acceleration near the QSL requires an injection energy ~ 0.01 MeV/nuc such that particles can move upstream and then, through multiple encounters of particles moving upstream and downstream, interact with the QSL repeatedly.

The structures created by reconnection near the QSL cascade down in size as they interact with the surrounding solar wind, driving energy from larger to smaller scales. At energies below the injection energy, particles interact with and are accelerated by these meso-scale structures and small-scale structures in the solar wind. Because these smaller structures move out in the reference frame of the solar wind, there is no required injection, and particles are accelerated down to the core of the solar wind. Appendix C treats the acceleration in meso-scale and small-scale structures as a superposition of stochastic processes (Schwadron et al. 2010a), resulting in the distribution function,

$$f_{\text{inject}}(v > c_s) = \left(\frac{n}{2\pi v^2} \right) \frac{\zeta_0}{(v\zeta_0 + 1)^3}, \quad (10)$$

where n is the density of the plasma, and the distribution function is explicitly considered for particle speeds greater than the core or thermal speed of the distribution, $v > c_s$. The quantity ζ_0 represents an inverse mean speed

characteristic of superposed distributions. The superposition sums weighted exponential probability distributions, $\exp(-\zeta v)$, each with different exponential roll-overs at inverse speed ζ . The array of these weighted probability distributions are characteristic as states in a system, and the weights are determined from the maximization of Boltzmann entropy (Schwadron et al. 2010a) with the constraint of mean inverse speed ζ_0 . The acceleration of particles associated with the states in the system are driven by momentum diffusion, with rate

$$D_{pp}^\ell = \frac{\ell}{L} D_{pp} \quad (11)$$

that is scaled based on the size ℓ of the meso- or small-scale structure versus the size L of the larger-scale QSL. The inverse mean speed ζ_0 is therefore related to the timescale of interaction ℓ/c_s multiplied by the diffusion rate $D_{pp}^\ell(c_s)$ evaluated near the sound speed of the plasma,

$$\frac{1}{\zeta_0} = \sqrt{\frac{D_{pp}^\ell(c_s)}{m^2} \frac{\ell}{c_s}}. \quad (12)$$

The distribution function $f_{\text{inject}}(v > c_s)$ in Equation 10 represents the population of particles injected into higher energy acceleration near the QSL.

Figure 11 shows the calculated distributions above the injection energy. The amplitudes of the differential fluxes are determined by the injected particles accelerated by meso-scale (and small-scale) structures, and the subsequent acceleration in the large-scale QSL at energies greater than the injection energy. We have taken a plasma density n projected to the QSL near $3 R_\odot$ from the location of PSP (0.8 au) using a density at PSP of roughly 5 cm^{-3} . The transition from small-scale to meso-scale structure is at the size of $\ell \approx 5 \text{ Mm}$ based on observations (Viall et al. 2021). This transition occurs between the solar wind kinetic scales and the meso-scale structures that begin to form in the spatial range of $\ell > 5 \text{ Mm}$.

Also shown in Figure 11 is the seed spectrum (black dashed curve) used for event modeling. This seed spectrum was fit to PSP EPI-Lo and EPI-Hi average proton fluxes during the pre-event period 00:00 – 10:00 UTC on November 29, 2020, using the following form,

$$J_{\text{seed}}(E, r = r_0) = J_0 \left(\frac{E}{E_0} \right)^{-\gamma} \exp\left(-\frac{E}{E_c}\right) \quad (13)$$

and the seed spectrum is projected to the QSL near $3 R_\odot$ based on a $1/r^\beta$ radial dependence. The fit to observations yields $J_0 = 4.8 \text{ particles}/(\text{cm}^2\text{-s-sr-MeV})$, $\gamma = 2.4$, $E_c = 1.6 \text{ MeV}$, and we have taken a standard square-radial distance scaling, $\beta = 2$. Figure 12 show the observed flux values along with a non-linear least squares fit of Equation 13 to the observations. Curve fitting was performed using `scipy.optimize.curve_fit` from SciPy version 1.6 (Virtanen et al. 2020).

3.5. Composition of seed populations from the QSL

The reviews by Gosling (1993) and Gosling et al. (1994) showed broad observational evidence indicating that CMEs are a unifier for our understanding of the non-recurrent disturbances that disrupt the magnetosphere and drive geomagnetic storms. These events cause the prompt acceleration of SEPs, which pose radiation risks (e.g., Schwadron et al. 2010b, 2014b) for astronauts and widespread problems for spacecraft and the instruments they carry. Large $\mathbf{J} \times \mathbf{B}$ forces form within magnetic flux tubes driven out of their quasi-equilibrium configurations in the corona during CME eruption and acceleration. The $\mathbf{J} \times \mathbf{B}$ forces within the CME cause the acceleration of the plasma, and this acceleration, in turn, drives the development of traveling shocks in the heliosphere. The shocks are known sites of rapid particle acceleration (e.g. Li et al. 2009; Schwadron et al. 2015).

Particle energization begins low in the corona during the fast expansion of a CME. The rapid particle acceleration is associated with the development of first compression regions and then shocks near the legs of the CME (Gorby et al. 2012; Linker et al. 2014; Schwadron et al. 2014c). An important feature of the structures that accelerate particles from the low corona is the buildup of the quasi perpendicular field compression at the front of the CME expansion. The fact that this sheath is draped by magnetic fields containing the plasma that is swept up by the CME suggests that this region should be effective at storing particle populations released prior to the CME injection. Therefore, these sheaths may naturally build up ^3He and heavy ions (e.g., O, Si, Fe) released by flares. Subsequent acceleration near

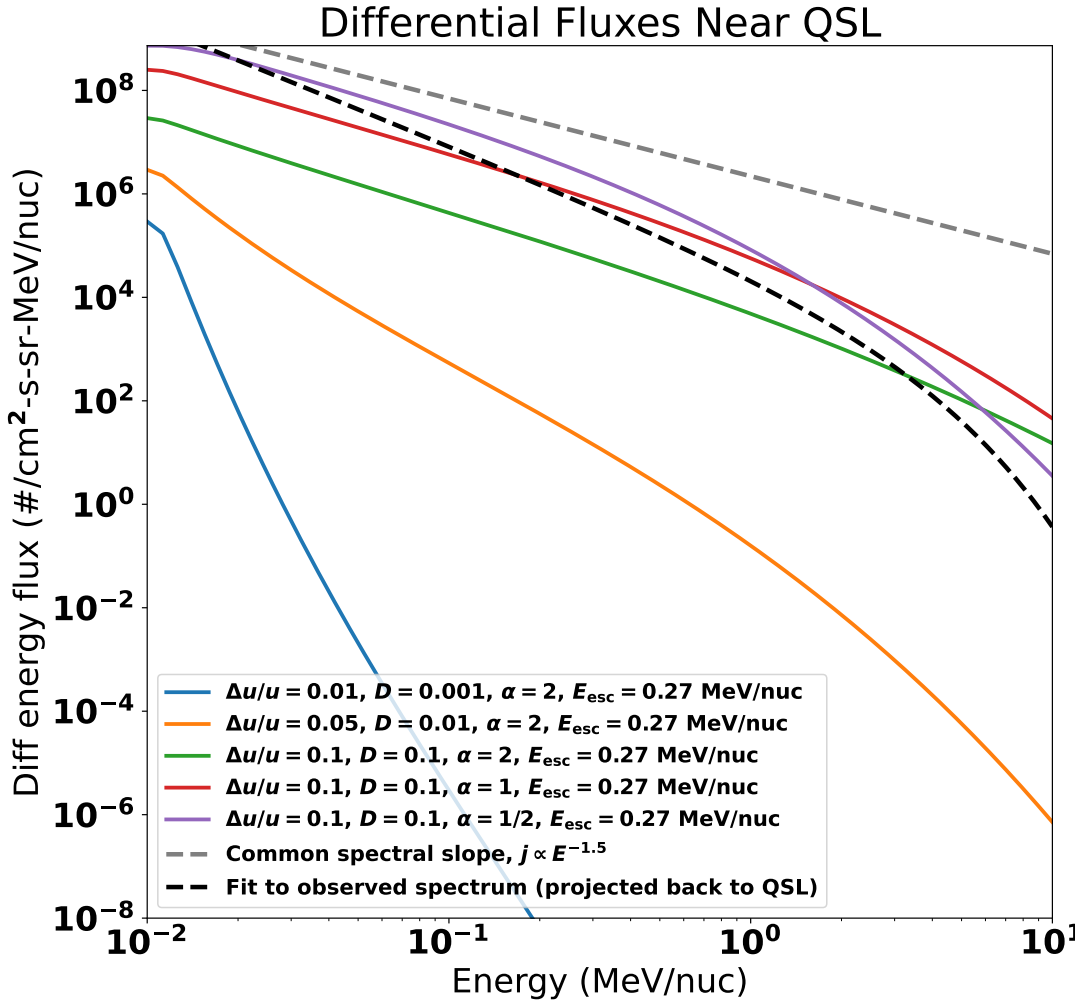


Figure 11. Differential fluxes associated with particle acceleration near QSLs. Curves are shown as a function of energy for various levels of diffusive acceleration, momentum diffusion, and the scaling of diffusion with momentum as detailed in the appendix. The amplitude of the differential fluxes is tied to the injection of particles accelerated from meso-scale and small-scale structures in the solar wind. High levels of diffusion converge to a common spectrum beneath the escape energy with differential energy flux proportional to $E^{-1.5}$ (see top grey dashed line). Low levels of diffusion result in a very soft spectrum, with relatively low differential fluxes. Also shown is the seed spectrum used for modeling near the QSL at $3 R_{\odot}$. This seed spectrum is fit from PSP observations at 0.8 au and projected back to the QSL near the Sun.

the shock or compression thereby enhances the suprathermal and energetic particle populations that build up within the sheath. Observations by the Integrated Science Investigation of the Sun (McComas et al. 2019) show precisely this process. The draped fields in front of a CME build up the energetic populations of charged particles from the surrounding plasma (Schwadron et al. 2020).

It is important to note that the pre-existing seed populations were hypothesized as the result of an array of flares or nanoflares ongoing at the Sun (Parker 1988). The presence of enhanced ^3He throughout observed events provides direct evidence that flares contribute to energetic particle seed populations (Mason et al. 1986; Mason et al. 2002; Reames 1999; Desai et al. 2003). The intertwining of flares as seed populations, subsequent compressive build-up (pre-conditioning) of these populations, and then higher energy acceleration as strong compressions and shocks form further out in the heliosphere supports the unifying role of the CME, together with an important role for flaring in producing energetic particle seed populations.

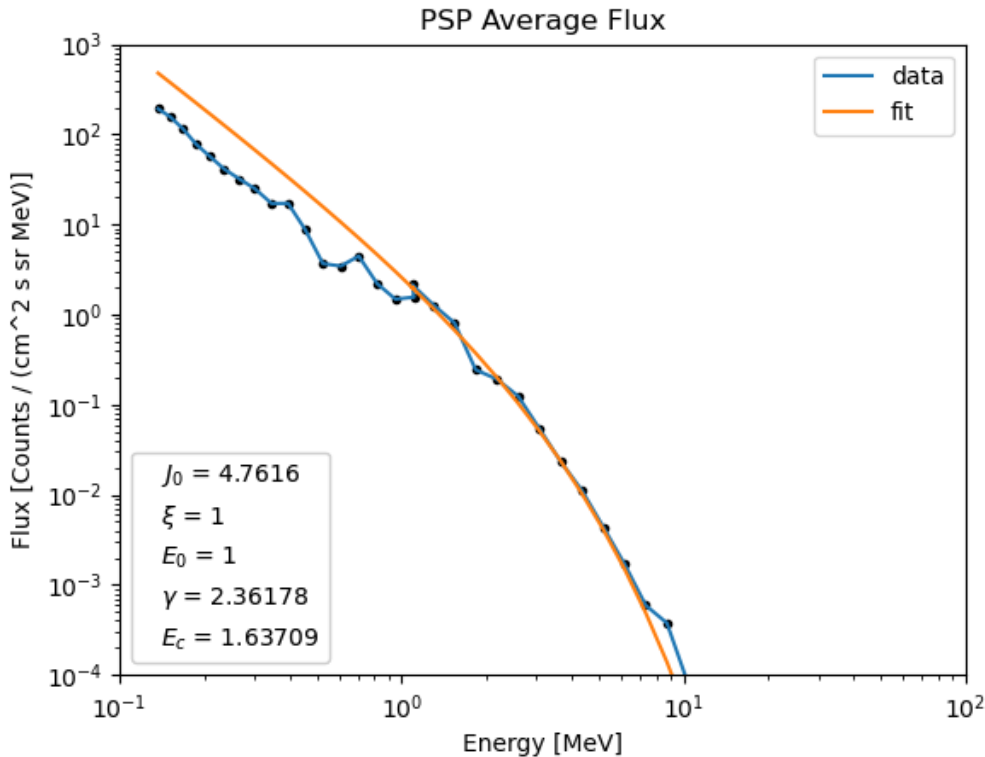


Figure 12. Observed proton fluxes from PSP/EPI-Lo and PSP/EPI-Hi (black dots with blue line) and fit to the analytic form of the seed-spectrum equation used in EPREM. The legend in the lower left gives the values of equation parameters.

Recent work (Mitchell et al. 2020) studied a solar energetic particle event observed by IS \odot IS during PSP’s first orbit (day-of-year 314–316, 2018) associated with the release of a slow coronal mass ejection close to the Sun (~ 0.23 au). This study likened the event with the energetic particle population produced in high current density structures associated with auroral phenomena in planetary magnetospheres. In this “auroral pressure cooker” mechanism, an electric field is associated with strong parallel currents that participate in driving a broadband distribution of waves. These waves, in turn, accelerate ions over wide-ranging charge/mass ratios. Temerin & Roth (1992) compared auroral plasmas with flare-associated plasmas, concluding that ion heating from resonances with electromagnetic ion cyclotron (EMIC) waves should energize particles efficiently in the Sun’s corona.

The acceleration detailed in this manuscript is driven by magnetic reconnection at QSLs. The reconfiguration of the magnetic field is naturally similar to a flaring process, and may be associated with or even create the conditions for sympathetic flaring at the footpoints of fieldlines tied to the QSL. The reconnection process also releases material previously contained within closed magnetic field structures, which are often rich in heavy ions and would store ^3He enriched plasma. Therefore, the seed population produced by QSLs is expected to be rich in ^3He and heavy ions.

The build-up of heavy ions on closed field structures was recently corroborated by direct observations from PSP (Schwadron et al. 2024). PSP/IS \odot IS at ~ 0.2 au on March 2, 2022 observed an event in which there was rare coincidence between imaging and in situ measurements. During this event, PSP passed through structures on the flank of a streamer-blowout CME including an isolated flux tube in front of the CME, a turbulent sheath, and the CME itself. The isolated flux tube shows large streaming, hard spectra, and large Fe/O and He/H ratios, indicating flare sources. Energetic particle fluxes are most enhanced within the CME interval from suprathermal through energetic particle energies (keV to > 10 MeV), indicating particle acceleration, as well as confinement local to the closed magnetic structure. The flux-rope morphology of the CME helps to enable local modulation and trapping of energetic particles. The closed field structure of the CME acts to build up energetic particle populations.

The CME observed by Schwadron et al. (2024) corroborates the build-up of suprathermal and energetic particle seed populations with heavy ion enhancements on closed field structures. Within the QSL reconnection regions, we therefore expect the release of seed populations that have elevated levels of heavy ions.

4. CONCLUSION

This is the first paper to show energetic particle simulations near the Sun at QSLs indicating particle acceleration in the exhausts associated with magnetic interchange reconnection between open magnetic field lines and closed structures. In recent simulations of CMEs with MAS coupled to EPREM, common sources of energetic particles were discovered over broad longitudinal distributions in the background solar wind, far from the sites of particle acceleration driven by the compressions and shocks in front of CMEs.

An important property of the QSL regions studied is that the reconnection process naturally re-configures the coronal magnetic field, and may drive sympathetic flaring near the Sun. The interchange reconnection process releases suprathermal particles previously stored on closed magnetic structures. Both the connection to flaring and the release of previously stored plasma on closed magnetic structures indicates that seed populations accelerated in QSLs should be rich in ^3He and heavy ions.

The energy released from magnetic reconnection near the QSL drives field-aligned flows, which in turn accelerate SEPs. Thus, we present the first global simulations of energetic particles accelerated from QSLs and above current sheets at the Sun. Our results provide a plausible source for energetic particle seed populations near the Sun, which likely have ^3He and heavy ion enhancements. These results aid in the development of predictive SEP models (see, e.g., the review by Whitman et al. 2023).

ACKNOWLEDGEMENTS

The authors would like to thank T. Forbes for discussions, almost a decade before submission, that helped to formulate ideas used in the manuscript. The authors would like to thank T. Lim and C.-M. Um for checking the derivation of the transport equation in Appendix A. Support for the project was provided by NASA's LWS-SC (grant no. 80NSSC22K0893) and LWS (grant no. 80NSSC19K0067) programs.

REFERENCES

- Aly, J. J. 1990, *Comput. Phys. Commun.*, 59, 13, doi: [10.1016/0010-4655\(90\)90152-Q](https://doi.org/10.1016/0010-4655(90)90152-Q)
- Anastasiadis, A., Lario, D., Papaioannou, A., Kouloumvakos, A., & Vourlidis, A. 2019, *Philosophical Transactions of the Royal Society of London Series A*, 377, 20180100, doi: [10.1098/rsta.2018.0100](https://doi.org/10.1098/rsta.2018.0100)
- Antiochos, S. K., Mikić, Z., Titov, V. S., Lionello, R., & Linker, J. A. 2011, *ApJ*, 731, 112, doi: [10.1088/0004-637X/731/2/112](https://doi.org/10.1088/0004-637X/731/2/112)
- Axford, W. I. 1977, in *Study of Traveling Interplanetary Phenomena*, ed. M. A. Schea, D. F. Smart, & S.-T. Wu (Norwell, Mass: D. Reidel), 145
- Bagalá, L., Mandrini, C., Rovira, M., & Démoulin, P. 2000, *Astronomy and Astrophysics*, 363, 779
- Baker, D., Démoulin, P., Yardley, S. L., et al. 2023, *ApJ*, 950, 65, doi: [10.3847/1538-4357/acc653](https://doi.org/10.3847/1538-4357/acc653)
- Baum, P. J., & Bratenahl, A. 1980, *Solar Phys.*, 67, 245, doi: [10.1007/BF00149805](https://doi.org/10.1007/BF00149805)
- Blackman, E. G., & Field, G. B. 1994, *Phys. Rev. Lett.*, 73, 3097, doi: [10.1103/PhysRevLett.73.3097](https://doi.org/10.1103/PhysRevLett.73.3097)
- Chitta, L. P., Seaton, D. B., Downs, C., DeForest, C. E., & Higginson, A. K. 2023, *Nature Astronomy*, 7, 133, doi: [10.1038/s41550-022-01834-5](https://doi.org/10.1038/s41550-022-01834-5)
- Cohen, C. M. S., Christian, E. R., Cummings, A. C., et al. 2021, *A&A*, 656, A29, doi: [10.1051/0004-6361/202140967](https://doi.org/10.1051/0004-6361/202140967)
- Crooker, N. U., Gosling, J. T., & Kahler, S. W. 2002, *Journal of Geophysical Research (Space Physics)*, 107, 1028, doi: [10.1029/2001JA000236](https://doi.org/10.1029/2001JA000236)
- Dayeh, M. A., Desai, M. I., Dwyer, J. R., et al. 2009, *Astrophys. J.*, 693, 1588, doi: [10.1088/0004-637X/693/2/1588](https://doi.org/10.1088/0004-637X/693/2/1588)
- Démoulin, P., Bagala, L. G., Mandrini, C. H., Henoux, J. C., & Rovira, M. G. 1997, *A&A*, 325, 305
- Démoulin, P., Henoux, J.-C., Priest, E., & Mandrini, C. 1996, *Astronomy and Astrophysics*, 308, 643
- Démoulin, P., Priest, E., & Lonie, D. 1996, *Journal of Geophysical Research: Space Physics*, 101, 7631
- Desai, M. I., Mason, G. M., Dwyer, J. R., et al. 2003, *Astrophys. J.*, 588, 1149, doi: [10.1086/374310](https://doi.org/10.1086/374310)
- Downs, C., Linker, J. A., Mikić, Z., et al. 2013, *Science*, 340, 1196, doi: [10.1126/science.1236550](https://doi.org/10.1126/science.1236550)

- Dragulescu, A., & Yakovenko, V. M. 2000, "Eur. Phys. J. B, 17, 723
- Dresing, N., Gómez-Herrero, R., Klassen, A., et al. 2012, *SoPh*, 281, 281, doi: [10.1007/s11207-012-0049-y](https://doi.org/10.1007/s11207-012-0049-y)
- Dresing, N., Rodríguez-García, L., Jebaraj, I. C., et al. 2023, *A&A*, 674, A105, doi: [10.1051/0004-6361/202345938](https://doi.org/10.1051/0004-6361/202345938)
- Dröge, W. 2000, *Astrophys. J.*, 537, 1073, doi: [10.1086/309080](https://doi.org/10.1086/309080)
- Fisk, L. A., & Gloeckler, G. 2008, *Astrophys. J.*, 686, 1466, doi: [10.1086/591543](https://doi.org/10.1086/591543)
- Fisk, L. A., Gloeckler, G., & Schwadron, N. A. 2010, *Astrophys. J.*, 720, 533, doi: [10.1088/0004-637X/720/1/533](https://doi.org/10.1088/0004-637X/720/1/533)
- Fisk, L. A., & Schwadron, N. A. 2001, *Astrophys. J.*, 560, 425
- Forbes, T. G. 1986, *Astrophys. J.*, 305, 553, doi: [10.1086/164268](https://doi.org/10.1086/164268)
- . 2000, *J. Geophys. Res.*, 105, 23153, doi: [10.1029/2000JA000005](https://doi.org/10.1029/2000JA000005)
- Forman, M. A. 1970, *Planet. & Space Sci.*, 18, 25
- Fox, N. J., Velli, M. C., Bale, S. D., et al. 2016, *Space Science Reviews*, 204, 7, doi: [10.1007/s11214-015-0211-6](https://doi.org/10.1007/s11214-015-0211-6)
- Giacalone, J., & Jokipii, J. R. 1999, *Astrophys. J.*, 520, 204, doi: [10.1086/307452](https://doi.org/10.1086/307452)
- Giacalone, J., Cohen, C. M. S., McComas, D. J., et al. 2023, *ApJ*, 958, 144, doi: [10.3847/1538-4357/acfb86](https://doi.org/10.3847/1538-4357/acfb86)
- Gorby, M. J., Schwadron, N. A., Linker, J. A., et al. 2012, *AGU Fall Meeting Abstracts*, A2216
- Gosling, J. T. 1993, *J. Geophys. Res.*, 98, 18937, doi: [10.1029/93JA01896](https://doi.org/10.1029/93JA01896)
- Gosling, J. T., Bame, S. J., McComas, D. J., et al. 1994, *Geophys. Res. Lett.*, 21, 237
- Gosling, J. T., Birn, J., & Hesse, M. 1995, *Geophys. Res. Lett.*, 22, 869
- Green, L. M., Török, T., Vršnak, B., Manchester, W., & Veronig, A. 2018, *SSRv*, 214, 46, doi: [10.1007/s11214-017-0462-5](https://doi.org/10.1007/s11214-017-0462-5)
- Henoux, J., & Somov, B. 1987, *Astronomy and Astrophysics (ISSN 0004-6361)*, 185, 306
- Higginson, A. K., Antiochos, S. K., DeVore, C. R., Wyper, P. F., & Zurbuchen, T. H. 2017, *ApJL*, 840, L10, doi: [10.3847/2041-8213/aa6d72](https://doi.org/10.3847/2041-8213/aa6d72)
- Higginson, A. K., & Lynch, B. J. 2018, *ApJ*, 859, 6, doi: [10.3847/1538-4357/aabc08](https://doi.org/10.3847/1538-4357/aabc08)
- Hill, M. E., Schwadron, N. A., Hamilton, D. C., Di Fabio, R. D., & Squier, R. K. 2009, *Astrophys. J. Lett.*, 699, L26, doi: [10.1088/0004-637X/699/1/L26](https://doi.org/10.1088/0004-637X/699/1/L26)
- Kallenrode, M. B., Wibberenz, G., & Hucke, S. 1992, *Astrophys. J.*, 394, 351, doi: [10.1086/171587](https://doi.org/10.1086/171587)
- Khoo, L. Y., Sánchez-Cano, B., Lee, C. O., et al. 2024, *ApJ*, 963, 107, doi: [10.3847/1538-4357/ad167f](https://doi.org/10.3847/1538-4357/ad167f)
- Kollhoff, A., Kouloumvakos, A., Lario, D., et al. 2021, *A&A*, 656, A20, doi: [10.1051/0004-6361/202140937](https://doi.org/10.1051/0004-6361/202140937)
- Kóta, J., Manchester, W. B., Jokipii, J. R., de Zeeuw, D. L., & Gombosi, T. I. 2005, in *American Institute of Physics Conference Series*, Vol. 781, *The Physics of Collisionless Shocks: 4th Annual IGPP International Astrophysics Conference*, ed. G. Li, G. P. Zank, & C. T. Russell, 201–206, doi: [10.1063/1.2032697](https://doi.org/10.1063/1.2032697)
- Kouloumvakos, A., Kwon, R. Y., Rodríguez-García, L., et al. 2022, *A&A*, 660, A84, doi: [10.1051/0004-6361/202142515](https://doi.org/10.1051/0004-6361/202142515)
- Kozarev, K. A., Evans, R. M., Schwadron, N. A., et al. 2013, *Astrophys. J.*, 778, 43, doi: [10.1088/0004-637x/778/1/43](https://doi.org/10.1088/0004-637x/778/1/43)
- Lario, D., Kwon, R. Y., Vourlidis, A., et al. 2016, *ApJ*, 819, 72, doi: [10.3847/0004-637X/819/1/72](https://doi.org/10.3847/0004-637X/819/1/72)
- Lau, Y.-T. 1993, *Solar physics*, 148, 301
- Li, G., Zank, G. P., Verkhoglyadova, O., et al. 2009, *Astrophys. J.*, 702, 998, doi: [10.1088/0004-637X/702/2/998](https://doi.org/10.1088/0004-637X/702/2/998)
- Linker, J., Mikic, Z., Schwadron, N., et al. 2014, in *COSPAR Meeting*, Vol. 40, *40th COSPAR Scientific Assembly*, 1840
- Linker, J. A., Caplan, R. M., Schwadron, N., et al. 2019, in *Journal of Physics Conference Series*, Vol. 1225, *Journal of Physics Conference Series*, 012007, doi: [10.1088/1742-6596/1225/1/012007](https://doi.org/10.1088/1742-6596/1225/1/012007)
- Linker, J. A., Lionello, R., Mikić, Z., Titov, V. S., & Antiochos, S. K. 2011, *Astrophys. J.*, 731, 110, doi: [10.1088/0004-637X/731/2/110](https://doi.org/10.1088/0004-637X/731/2/110)
- Linker, J. A., Torok, T., Downs, C., et al. 2024, *Journal of Physics Conference Series*, 2742, 012012, doi: [10.1088/1742-6596/2742/1/012012](https://doi.org/10.1088/1742-6596/2742/1/012012)
- Linker, J. A., Mikić, Z., Biasecker, D. A., et al. 1999, *J. Geophys. Res.*, 104, 9809, doi: [10.1029/1998JA900159](https://doi.org/10.1029/1998JA900159)
- Linker, J. A., Caplan, R. M., Downs, C., et al. 2017, *ApJ*, 848, 70, doi: [10.3847/1538-4357/aa8a70](https://doi.org/10.3847/1538-4357/aa8a70)
- Lionello, R., Downs, C., Linker, J. A., et al. 2013, *Astrophys. J.*, 777, 76, doi: [10.1088/0004-637X/777/1/76](https://doi.org/10.1088/0004-637X/777/1/76)
- Lionello, R., Linker, J. A., & Mikić, Z. 2009, *Astrophys. J.*, 690, 902, doi: [10.1088/0004-637X/690/1/902](https://doi.org/10.1088/0004-637X/690/1/902)
- Low, B., & Wolfson, R. 1988, *Astrophysical Journal*, Part 1 (ISSN 0004-637X), vol. 324, Jan. 1, 1988, p. 574-581., 324, 574
- Mandrini, C., Démoulin, P., Bagala, L., et al. 1997, *Solar Physics*, 174, 229
- Mason, G. M., Reames, D. V., Klecker, B., & Hovestadt, D. 1986, *Astrophys. J.*, 303, 849

- Mason, G. M., Wiedenbeck, M. E., Miller, J. A., et al. 2002, *Astrophys. J.*, 574, 1039, doi: [10.1086/341112](https://doi.org/10.1086/341112)
- McComas, D. J., Alexander, N., Angold, N., et al. 2016, *Space Sci. Rev.*, 204, 187, doi: [10.1007/s11214-014-0059-1](https://doi.org/10.1007/s11214-014-0059-1)
- McComas, D. J., Christian, E. R., Cohen, C. M. S., et al. 2019, *Nature*, 576, 223, doi: [10.1038/s41586-019-1811-1](https://doi.org/10.1038/s41586-019-1811-1)
- Mewaldt, R. A., Looper, M. D., Cohen, C. M. S., et al. 2012, *SSRv*, 171, 97, doi: [10.1007/s11214-012-9884-2](https://doi.org/10.1007/s11214-012-9884-2)
- Mikić, Z., & Linker, J. A. 1996, in *American Institute of Physics Conference Series*, Vol. 382, American Institute of Physics Conference Series, ed. D. Winterhalter, J. T. Gosling, S. R. Habbal, W. S. Kurth, & M. Neugebauer, 104–107, doi: [10.1063/1.51370](https://doi.org/10.1063/1.51370)
- Mikić, Z., Linker, J. A., Schnack, D. D., Lionello, R., & Tarditi, A. 1999, *Phys. Plasmas*, 6, 2217, doi: [10.1063/1.873474](https://doi.org/10.1063/1.873474)
- Mikić, Z., Downs, C., Linker, J. A., et al. 2018, *Nature Astronomy*, 2, 913, doi: [10.1038/s41550-018-0562-5](https://doi.org/10.1038/s41550-018-0562-5)
- Mitchell, D. G., Giacalone, J., Allen, R. C., et al. 2020, *Astrophys. J. Suppl.*, 246, 59, doi: [10.3847/1538-4365/ab63cc](https://doi.org/10.3847/1538-4365/ab63cc)
- Mitchell, J. G., De Nolfo, G. A., Hill, M. E., et al. 2021, *ApJ*, 919, 119, doi: [10.3847/1538-4357/ac110e](https://doi.org/10.3847/1538-4357/ac110e)
- Palmerio, E., Lee, C. O., Mays, M. L., et al. 2022, *Space Weather*, 20, e2021SW002993, doi: [10.1029/2021SW002993](https://doi.org/10.1029/2021SW002993)
- Parker, E. N. 1988, *Astrophys. J.*, 330, 474, doi: [10.1086/166485](https://doi.org/10.1086/166485)
- Priest, E. R., & Forbes, T. G. 2002, *Astron. Astrophys. Review*, 10, 313, doi: [10.1007/s001590100013](https://doi.org/10.1007/s001590100013)
- Reames, D. V. 1999, *Space Sci. Rev.*, 90, 413, doi: [10.1023/A:1005105831781](https://doi.org/10.1023/A:1005105831781)
- . 2013, *SSRv*, 175, 53, doi: [10.1007/s11214-013-9958-9](https://doi.org/10.1007/s11214-013-9958-9)
- Riley, P., Linker, J. A., Lionello, R., & Mikić, Z. 2012, *Journal of Atmospheric and Solar-Terrestrial Physics*, 83, 1, doi: [10.1016/j.jastp.2011.12.013](https://doi.org/10.1016/j.jastp.2011.12.013)
- Riley, P., Lionello, R., Linker, J. A., et al. 2011, *Solar Phys.*, 274, 361, doi: [10.1007/s11207-010-9698-x](https://doi.org/10.1007/s11207-010-9698-x)
- Ruffolo, D. 1995, *Astrophys. J.*, 442, 861, doi: [10.1086/175489](https://doi.org/10.1086/175489)
- Rygg, T. A., & Earl, J. A. 1971, *J. Geophys. Res.*, 76, 7445, doi: [10.1029/JA076i031p07445](https://doi.org/10.1029/JA076i031p07445)
- Schwadron, N. A., Dayeh, M. A., Desai, M., et al. 2010a, *Astrophys. J.*, 713, 1386, doi: [10.1088/0004-637X/713/2/1386](https://doi.org/10.1088/0004-637X/713/2/1386)
- Schwadron, N. A., Fisk, L. A., & Gloeckler, G. 1996, *GRL*, 23, 2871, doi: [10.1029/96GL02833](https://doi.org/10.1029/96GL02833)
- Schwadron, N. A., Fisk, L. A., & Zurbuchen, T. H. 1999, *Astrophys. J.*, 521, 859
- Schwadron, N. A., & Gombosi, T. I. 1994, *J. Geophys. Res.*, 99, 19301
- Schwadron, N. A., Townsend, L., Kozarev, K., et al. 2010b, *Space Weather*, 8, 0, doi: [10.1029/2009SW000523](https://doi.org/10.1029/2009SW000523)
- Schwadron, N. A., Gorby, M., Török, T., et al. 2014a, *Space Weather*, 12, 323, doi: [10.1002/2014SW001086](https://doi.org/10.1002/2014SW001086)
- Schwadron, N. A., Blake, J. B., Case, A. W., et al. 2014b, *Space Weather*, 12, 622, doi: [10.1002/2014SW001084](https://doi.org/10.1002/2014SW001084)
- Schwadron, N. A., Gorby, M., Török, T., et al. 2014c, *Space Weather*, 12, 323, doi: [10.1002/2014SW001086](https://doi.org/10.1002/2014SW001086)
- Schwadron, N. A., Lee, M. A., Gorby, M., et al. 2015, *Astrophys. J.*, 810, 97, doi: [10.1088/0004-637X/810/2/97](https://doi.org/10.1088/0004-637X/810/2/97)
- Schwadron, N. A., Bale, S., Bonnell, J., et al. 2020, *Astrophys. J. Suppl.*, 246, 33, doi: [10.3847/1538-4365/ab5527](https://doi.org/10.3847/1538-4365/ab5527)
- Schwadron, N. A., Bale, S. D., Bonnell, J., et al. 2024, *Astrophys. J.*, 970, 98, doi: [10.3847/1538-4357/ad527f](https://doi.org/10.3847/1538-4357/ad527f)
- Skilling, J. 1971, *Astrophys. J.*, 170, 265, doi: [10.1086/151210](https://doi.org/10.1086/151210)
- Somov, B. V., & Kosugi, T. 1997, *Astrophys. J.*, 485, 859, doi: [10.1086/304449](https://doi.org/10.1086/304449)
- Somov, B. V., Kosugi, T., & Sakao, T. 1998, *The Astrophysical Journal*, 497, 943, doi: [10.1086/305492](https://doi.org/10.1086/305492)
- Temerin, M., & Roth, I. 1992, *Astrophys. J. Lett.*, 391, L105, doi: [10.1086/186408](https://doi.org/10.1086/186408)
- Titov, V. S., Downs, C., Mikić, Z., et al. 2018, *The Astrophysical Journal Letters*, 852, L21, doi: [10.3847/2041-8213/aaa3da](https://doi.org/10.3847/2041-8213/aaa3da)
- Titov, V. S., Mikić, Z., Linker, J. A., Lionello, R., & Antiochos, S. K. 2011, *ApJ*, 731, 111, doi: [10.1088/0004-637X/731/2/111](https://doi.org/10.1088/0004-637X/731/2/111)
- Titov, V. S., Mikić, Z., Török, T., Linker, J. A., & Panasenco, O. 2017, *ApJ*, 845, 141, doi: [10.3847/1538-4357/aa81ce](https://doi.org/10.3847/1538-4357/aa81ce)
- Török, T., Downs, C., Linker, J. A., et al. 2018, *The Astrophysical Journal*, 856, 75
- Tsuneta, S., & Naito, T. 1998, *Astrophys. J. Lett.*, 495, L67, doi: [10.1086/311207](https://doi.org/10.1086/311207)
- Viall, N. M., DeForest, C. E., & Kepko, L. 2021, *Frontiers in Astronomy and Space Sciences*, 8, 139, doi: [10.3389/fspas.2021.735034](https://doi.org/10.3389/fspas.2021.735034)
- Virtanen, P., Gommers, R., Oliphant, T. E., et al. 2020, *Nature Methods*, 17, 261, doi: [10.1038/s41592-019-0686-2](https://doi.org/10.1038/s41592-019-0686-2)
- Švestka, Z. F., Fontenla, J. M., Machado, M. E., et al. 1987, *Solar Phys.*, 108, 237
- Wheatland, M. S. 2000, *Astrophys. J. Lett.*, 536, L109, doi: [10.1086/312739](https://doi.org/10.1086/312739)
- Whitman, K., Egeland, R., Richardson, I. G., et al. 2023, *Advances in Space Research*, 72, 5161, doi: [10.1016/j.asr.2022.08.006](https://doi.org/10.1016/j.asr.2022.08.006)

- Williams, L. L., Schwadron, N., Jokipii, J. R., & Gombosi, T. I. 1993, *Astrophys. J. Lett.*, 405, L79, doi: [10.1086/186770](https://doi.org/10.1086/186770)
- Workman, J. C., Blackman, E. G., & Ren, C. 2011, *Physics of Plasmas*, 18, 092902, doi: [10.1063/1.3631795](https://doi.org/10.1063/1.3631795)
- Yakovenko, V. M., & Rosser, Jr., J. B. 2009, "Reviews of Modern Physics", 81, 1703
- Young, M. A., Schwadron, N. A., Gorby, M., et al. 2021, *ApJ*, 909, 160, doi: [10.3847/1538-4357/abdf5f](https://doi.org/10.3847/1538-4357/abdf5f)
- Zank, G. P., Li, G., Florinski, V., et al. 2006, *Journal of Geophysical Research (Space Physics)*, 111, 6108, doi: [10.1029/2005JA011524](https://doi.org/10.1029/2005JA011524)

APPENDIX

A. FOCUSED TRANSPORT, ACCELERATION

The focused transport equation is

$$\begin{aligned} \frac{df}{dt} + v\mu\hat{e}_b \cdot \nabla f + \frac{1-\mu^2}{2} \left[-v\hat{e}_b \cdot \nabla \ln B - \frac{2}{v}\hat{e}_b \cdot \frac{d\mathbf{u}}{dt} + \mu \frac{d \ln n^2/B^3}{dt} \right] \frac{\partial f}{\partial \mu} \\ + \left[-\frac{\mu}{v}\hat{e}_b \cdot \frac{d\mathbf{u}}{dt} + \mu^2 \frac{d \ln n/B}{dt} + \frac{1-\mu^2}{2} \frac{d \ln B}{dt} \right] \frac{\partial f}{\partial \ln p} \\ = \frac{\partial}{\partial \mu} \left(D_{\mu\mu} \frac{\partial f}{\partial \mu} \right). \end{aligned} \quad (\text{A1})$$

The regions studied are exhausts from reconnection regions. Unlike reconnection regions in supersonic solar wind, these reconnection exhausts are consistent with a slow down in the flow along the flux tube, but in most regions the expansion in the flux tube roughly compensates the slow down in the wind to yield an almost constant density and a local reduction in magnetic flux through the exhaust region. Evaluation of acceleration terms indicates the dominance of terms involving $d \ln B/dt$, with some but comparatively modest changes in $d \ln n/dt$. Based on this analysis, we consider the following approximation to the focused transport equation:

$$\begin{aligned} \frac{df}{dt} + v\mu\hat{e}_b \cdot \nabla f - \frac{1-\mu^2}{2} \left[v\hat{e}_b \cdot \nabla \ln B + 3\mu \frac{d \ln(B/n^{2/3})}{dt} \right] \frac{\partial f}{\partial \mu} \\ + \left[\frac{1}{3} \frac{d \ln n}{dt} - \frac{3\mu^2-1}{2} \frac{d \ln(B/n^{2/3})}{dt} \right] \frac{\partial f}{\partial \ln p} \\ = \frac{\partial}{\partial \mu} \left(D_{\mu\mu} \frac{\partial f}{\partial \mu} \right). \end{aligned} \quad (\text{A2})$$

For the scattering coefficient, we use the following (Schwadron & Gombosi 1994):

$$D_{\mu\mu} = \frac{1-\mu^2}{2\tau_s}, \quad (\text{A3})$$

where τ_s^{-1} is the scattering rate, and τ_s is related to the parallel scattering mean free path, $\lambda_{\parallel} = \tau_s v$.

We now take moments of the distribution function assuming a truncated Legendre expansion:

$$f \approx f_0 P_0 + f_1 P_1(\mu) + f_2 P_2(\mu), \quad (\text{A4})$$

where P_i are Legendre Polynomials

$$\begin{aligned} P_0 &= 1, \\ P_1 &= \mu, \\ P_2 &= (3\mu^2 - 1)/2. \end{aligned}$$

We take the 0th-moment of equation (A2) by integrating the over the equation by $1/2 \int_{-1}^1 d\mu$, resulting in the following:

$$\begin{aligned} \frac{df_0}{dt} + \frac{v}{3}\hat{e}_b \cdot \nabla f_1 - \frac{v}{3}(\hat{e}_b \cdot \nabla \ln B) f_1 - \frac{3}{5} \frac{d \ln(B/n^{2/3})}{dt} f_2 - \frac{1}{5} \frac{d \ln(B/n^{2/3})}{dt} \frac{\partial f_2}{\partial \ln p} \\ + \frac{1}{3} \frac{d \ln n}{dt} \frac{\partial f_0}{\partial \ln p} = 0. \end{aligned} \quad (\text{A5})$$

Similarly, we take the 1st-moment of equation (A2) by integrating over the equation by $3/2 \int_{-1}^1 d\mu\mu$, resulting in the following:

$$\begin{aligned} \frac{df_1}{dt} + v\hat{e}_b \cdot \nabla \left(f_0 + \frac{2}{5} f_2 \right) - \frac{3v}{5} (\hat{e}_b \cdot \nabla \ln B) f_2 - \frac{3}{5} \frac{d \ln(B/n^{2/3})}{dt} f_1 - \frac{2}{5} \frac{d \ln(B/n^{2/3})}{dt} \frac{\partial f_1}{\partial \ln p} \\ + \frac{1}{3} \frac{d \ln n}{dt} \frac{\partial f_1}{\partial \ln p} = -\frac{f_1}{\tau_s}. \end{aligned} \quad (\text{A6})$$

We take the 2nd-moment of equation (A2) by integrating over the equation by $5/2 \int_{-1}^1 d\mu P_2(\mu)$, resulting in the following:

$$\begin{aligned} \frac{df_2}{dt} + \frac{2v}{3} \hat{e}_b \cdot \nabla f_1 + \frac{v}{3} \hat{e}_b \cdot \nabla \ln B f_1 - \frac{3}{7} \frac{d \ln(B/n^{2/3})}{dt} f_2 - \frac{d \ln(B/n^{2/3})}{dt} \frac{\partial f_0}{\partial \ln p} \\ - \frac{2}{7} \frac{d \ln(B/n^{2/3})}{dt} \frac{\partial f_2}{\partial \ln p} + \frac{1}{3} \frac{d \ln n}{dt} \frac{\partial f_2}{\partial \ln p} = -\frac{3f_2}{\tau_s}. \end{aligned} \quad (\text{A7})$$

We use the conventional expansion in terms of a smallness parameter $\epsilon \sim \tau_s f'_0$ where f'_0 denotes the time differential $\partial f_0 / \partial t$, spatial differential $v \nabla f_0$, or other rates multiplied by terms involving f_0 . In other words, the expansion is about the scattering time, which defines the smallest timescale of the quantities considered. This leads to following approximations for f_1 and f_2 :

$$f_1 \approx -\lambda_{\parallel} \hat{e}_b \cdot \nabla f_0 \quad (\text{A8})$$

$$f_2 \approx \frac{\tau_s}{3} \frac{d \ln(B/n^{2/3})}{dt} \frac{\partial f_0}{\partial \ln p} \quad (\text{A9})$$

where $\lambda_{\parallel} = \tau_s v$ is the parallel scattering mean free path. Substituting these terms into the zeroth-moment equation (A5) yields:

$$\frac{df_0}{dt} - \nabla \cdot (\bar{\kappa} \cdot \nabla f_0) - \frac{\nabla \cdot \mathbf{u}}{3} \frac{\partial f_0}{\partial \ln p} - \frac{1}{p^2} \frac{\partial}{\partial p} \left(p^2 D_{pp} \frac{\partial f_0}{\partial p} \right) = 0. \quad (\text{A10})$$

where

$$\bar{\kappa} = \frac{\lambda_{\parallel} v}{3} \hat{e}_b \hat{e}_b \quad (\text{A11})$$

and

$$\frac{D_{pp}}{p^2} = \frac{\tau_s}{15} \left(\frac{d \ln(B/n^{2/3})}{dt} \right)^2. \quad (\text{A12})$$

Therefore, the effect of the QSL and current sheet reconnection regions is to create localized particle acceleration due to diffusion in momentum space. The diffusion coefficient resembles that derived from transit-time damping magnetic field fluctuations in field magnitude (Schwadron et al. 1996).

The form of acceleration derived here implies that particles experience energy changes through multiple interactions with the reconnection region. Particles passing directly through the reconnection region without scattering experience little or no change in energy after exiting the region, and without scattering, these particles cannot return to the reconnection region for further interactions. Scattering, therefore, is a critical part of the acceleration process, both for interrupting the adiabatic change process within the reconnection region, and for enabling particles to interact with the reconnection region over multiple encounters.

B. ACCELERATION AT A 2D STRUCTURE

Our approach to understanding the influence of structure on the evolution of distribution functions in the outflows of the quasi-separatrix layer utilizes the simplified transport equation (A10) as a starting point. We define the coefficient C (the Compton-Getting coefficient, Forman 1970; Rygg & Earl 1971) for the distribution function, and allow for changes in the power-law,

$$p \frac{\partial f_0}{\partial p} = -3C f_0. \quad (\text{B13})$$

We recast the transport equation in a conservative form:

$$\frac{\partial f_0}{\partial t} + \nabla \cdot (\mathbf{u} f_0) - \nabla \cdot (\bar{\kappa} \cdot \nabla f_0) + (C - 1) \nabla \cdot \mathbf{u} f_0 - \frac{1}{p^2} \frac{\partial}{\partial p} \left(p^2 D_{pp} \frac{\partial f_0}{\partial p} \right) = 0. \quad (\text{B14})$$

Here we take z as a linear coordinate along a magnetic field line, and the $z = 0$ position where the particles are fed into acceleration. Similarly, both the flow divergence ($\nabla \cdot \mathbf{u}$) and the momentum diffusion term ($\frac{1}{p^2} \frac{\partial}{\partial p} \left(p^2 D_{pp} \frac{\partial f_0}{\partial p} \right)$) are taken as localized acceleration at $z = 0$:

$$\nabla \cdot \mathbf{u} = -\Delta u \delta(z) = -(d \ln n / dt) L \delta(z) \quad (\text{B15})$$

$$D_{pp}/p^2 = D_0 L \delta(z). \quad (\text{B16})$$

Here L is the characteristic size of the acceleration region, Δu is the speed reduction across the interface, and

$$D_0 = \frac{\tau_s}{15} \left(\frac{d \ln(B/n^{2/3})}{dt} \right)^2 \quad (\text{B17})$$

We take what has become a standard approach to diffusive acceleration, by first integrating the distribution upstream of the acceleration region, where convection balances the back diffusion of accelerated ions:

$$u_{su} f_0 - \kappa_{\parallel} \frac{\partial f_0}{\partial z} = 0. \quad (\text{B18})$$

Here, u_{su} is the flow speed parallel to the magnetic field upstream from the discontinuity. The upstream solution readily follows

$$f_0 \propto f_a \exp(u_{su} z / \kappa_{\parallel}) \quad (\text{B19})$$

and downstream, $f_0 \approx f_a$. We have denoted f_a as the isotropic part of the distribution function associated with accelerated particles at the position of localized acceleration. Integrating across a small region local to the acceleration region, we recover the following

$$u_{su} f_a + \frac{\Delta u}{3} p \frac{\partial f_a}{\partial p} - \frac{1}{p^2} \frac{\partial}{\partial p} \left(p^4 D_0 L \frac{\partial f_a}{\partial p} \right) = 0 \quad (\text{B20})$$

Note that the acceleration process involves diffusion, and as the scattering mean free path approaches the scale of the acceleration region, particles experience an increased probability of escaping the acceleration process. We therefore include a loss term associated with escaping particles:

$$u_{su} f_a + \frac{\Delta u}{3} p \frac{\partial f_a}{\partial p} - \frac{1}{p^2} \frac{\partial}{\partial p} \left(p^4 D_0 L \frac{\partial f_a}{\partial p} \right) = -\frac{f_a}{\tau_{\text{esc}}} \quad (\text{B21})$$

where the loss-timescale is energy dependent, $\tau_{\text{esc}} = \tau_{\text{esc}}(E)$.

We proceed by first treating the problem of diffusive acceleration as a superposition of acceleration processes (§B.1), and then proceed to derive the more general solutions that include both diffusive shock acceleration and energy diffusion from the QSL layer (§B.2).

B.1. Diffusive Shock Acceleration As An Exponential Process

We include a refined approach to understanding diffusive acceleration as a superposition of processes. We show that the approach is consistent with a well-known diffusive acceleration solution, while also providing a methodology that allows the problem to be compared to other treatments for the superposition of stochastic processes (Schwadron et al. 2010a). Since we neglect diffusion, the following follows from equation (B21),

$$\frac{\partial f_a}{\partial t} + \frac{u_{su}}{L} f_a + \frac{\Delta u}{3L} p \frac{\partial f_a}{\partial p} = -\frac{f_a}{\tau_{\text{esc}}} \quad (\text{B22})$$

By retaining time-dependence, we gain insight into the acceleration process that is useful both in understanding the relationship between diffusive shock acceleration and superposed stochastic processes, and in deriving the solution that includes energy diffusion. In introducing time-dependence, we also must include a spatial scale L over which the diffusion acceleration process proceeds. This spatial scale is related to the diffusion coefficient and the upstream solar wind speed, as detailed by Schwadron et al. (2015).

It is convenient to introduce the following variables:

$$t_0 = L/u_{su} \quad (\text{B23})$$

$$s = t/t_0 \quad (\text{B24})$$

$$q = p/p_i \quad (\text{B25})$$

Here, p_i is the injection momentum. The dimensionless form of equation (B22) is,

$$\frac{\partial f_a}{\partial s} + f_a \left(1 + \frac{t_0}{\tau_{\text{esc}}}\right) + \frac{1}{\gamma} \frac{\partial f_a}{\partial \ln q} = 0. \quad (\text{B26})$$

where $\gamma = 3r_c/(r_c - 1) = 3u_{su}/(\Delta u)$ and $r_c = u_{su}/u_{sd}$ is the compression ratio.

An important feature of equation (B26) is that the acceleration proceeds along a characteristic:

$$q(s, s_i) = \exp[\Delta u(s - s_i)/(3u_{su})]. \quad (\text{B27})$$

where s_i is the time of particle injection. Taking $f_a = g \exp[-(s - s_i)(1 + t_0/\tau_{\text{esc}})]$ provides a simplification for treating the particle loss. We neglect momentum gradients of the escape timescale since these gradients are far smaller than the momentum gradient in the distribution function. Taking $g = g(s, q)$ yields the following,

$$\frac{\partial g}{\partial s} = 0 \quad (\text{B28})$$

Following the characteristic implies that

$$f_a = f_i \exp(-[s - s_i][1 + t_0/\tau_{\text{esc}}]) \quad (\text{B29})$$

where f_i is the distribution function at the injection energy. We can solve for $(s - s_i)$ from the characteristic,

$$s - s_i = \gamma \ln q \quad (\text{B30})$$

and

$$f_a = f_i \exp(-\gamma[1 + t_0/\tau_{\text{esc}}] \ln q) \quad (\text{B31})$$

$$= f_i (p/p_i)^{-\gamma[1 + t_0/\tau_{\text{esc}}]} \quad (\text{B32})$$

Thus, for no escape, we recover the standard diffusive shock acceleration power-law $f_a \propto p^{-\gamma}$. The more general case that includes escape leads to broken power-law distributions as discussed by Schwadron et al. (2015).

The result was derived using a model with time-dependent acceleration. This approach provides a deeper connection with stochastic processes, as detailed in §C.

B.2. Solution Including Energy Diffusion and Diffusive Shock Acceleration

We now take up the solution that incorporates both diffusive shock acceleration and energy diffusion. As in §B.1, we seek the steady-state limit, and time-dependence is considered as a means to simplify deriving analytic solutions. Therefore, the starting point is the following differential equation,

$$\frac{\partial f_a}{\partial t} + \frac{u_{su}}{L} f_a + \frac{\Delta u}{3Lp} \frac{\partial f_a}{\partial p} - \frac{1}{p^2} \frac{\partial}{\partial p} \left(p^4 D_0 \frac{\partial f_a}{\partial p} \right) = -\frac{f_a}{\tau_{\text{esc}}} \quad (\text{B33})$$

Our initial approach is similar to the treatment of diffusive shock acceleration. We take

$$f_a = g \exp(-[s - s_i][1 + t_0/\tau_{\text{esc}}]), \quad (\text{B34})$$

where $g = g(s, q)$, and neglect momentum gradients (as in §B.1) of the escape timescale since these gradients are far smaller than the momentum gradient in the distribution function. This substitution results in the following,

$$\frac{\partial g}{\partial s} + \frac{1}{\gamma} \frac{\partial g}{\partial \ln q} - t_0 \frac{1}{q^2} \frac{\partial}{\partial q} \left(q^4 D_0 \frac{\partial g}{\partial q} \right) = 0 \quad (\text{B35})$$

We now introduce generalized coordinates (s', q') that allow for acceleration along a characteristic, and diffusion across characteristics:

$$s' = s \quad (\text{B36})$$

$$q' = q \exp(-s/\gamma) \quad (\text{B37})$$

In these coordinates, equation (B35) becomes,

$$\frac{\partial g}{\partial s'} - t_0 \frac{1}{(q')^2} \frac{\partial}{\partial q'} \left((q')^4 D_0 \frac{\partial g}{\partial q'} \right) = 0 \quad (\text{B38})$$

The addition of energy diffusion allows for a diffusive spread of particles with momenta both above and below the characteristic momentum.

We consider power-law dependence for the diffusive constant,

$$t_0 D_0 = D q^\alpha \quad (\text{B39})$$

The following constants and variables are used to modify the diffusion term into a modified Bessel equation

$$d = -(1 + 6/\alpha) \quad (\text{B40})$$

$$y = \exp(s' \alpha / \gamma) \quad (\text{B41})$$

$$z = (q')^{-\alpha/2} \quad (\text{B42})$$

$$g = z^{(1-d)/2} h \quad (\text{B43})$$

which reduces equation (B38) into the following form:

$$\frac{\partial h}{\partial y} - \frac{\alpha \gamma D}{4} z^{-(1+d)/2} \frac{\partial}{\partial z} \left(z^d \frac{\partial}{\partial z} [z^{(1-d)/2} h] \right) = 0 \quad (\text{B44})$$

The solution for equation (B44) is found using a Hankel transform:

$$H_\nu(y, k) = \int_0^\infty h(y, z) J_\nu(kz) z dz \quad (\text{B45})$$

$$h(y, z) = \int_0^\infty H_\nu(y, k) J_\nu(kz) k dk \quad (\text{B46})$$

where J_ν is the standard Bessel's function of order ν . With $\nu = |1 - d|/2$, equation (B44) is an eigenfunction for the Bessel function, with the following Hankel transform

$$\frac{\partial H_\nu}{\partial y} + \frac{\alpha \gamma D k^2}{4} H_\nu = 0 \quad (\text{B47})$$

Therefore, the transform is

$$H_\nu(y, k) = H_\nu(y_i, k) \exp\left(-\frac{\alpha \gamma D k^2}{4} [y - y_i]\right) \quad (\text{B48})$$

$$= \exp\left(-\frac{\alpha \gamma D k^2}{4} [y - y_i]\right) \int_0^\infty h(y_i, z') J_\nu(kz') z' dz' \quad (\text{B49})$$

where the value $y = y_i$ corresponds to the initial condition. The corresponding solution is

$$h(y, z) = \int_0^\infty k dk J_\nu(kz) \exp\left(-\frac{\alpha \gamma D k^2}{4} [y - y_i]\right) \int_0^\infty h(y_i, z') J_\nu(kz') z' dz' \quad (\text{B50})$$

The particular solution of injection at $p = p_i$ implies a delta function for $h(y_i, z) = h_i \delta(z - z_i)$. Here, $z = \sqrt{y_i}$ is the initial condition since particles are injected from $q = 1$ and $z_i = (q'_i)^{-\alpha/2} = \sqrt{y_i}$. In this case, equation (B50) becomes

$$h(y, z) = h_i \int_0^\infty J_\nu(kz) J_\nu(kz_i) \exp\left(-\frac{\alpha \gamma D k^2}{4} [y - y_i]\right) k dk \quad (\text{B51})$$

$$= \left(\frac{2h_i}{\alpha \gamma D}\right) \frac{1}{(y - y_i)} \exp\left[-\left(\frac{1}{\alpha \gamma D}\right) \left(\frac{z^2 + z_i^2}{y - y_i}\right)\right] I_\nu\left[\left(\frac{2}{\alpha \gamma D}\right) \left(\frac{zz_i}{y - y_i}\right)\right] \quad (\text{B52})$$

Expressing the solution in terms of original variables $g(s, q)$ yields,

$$g = \left(\frac{2h_i}{\alpha\gamma D} \right) \frac{q^{-(3+\alpha)/2} \exp([s/\gamma][3+\alpha]/2)}{[\exp(s\alpha/\gamma) - \exp(s_i\alpha/\gamma)]} \\ \times \exp \left[- \left(\frac{1}{\alpha\gamma D} \right) \left(\frac{q^{-\alpha} \exp(s\alpha/\gamma) + \exp(s_i\alpha/\gamma)}{\exp(s\alpha/\gamma) - \exp(s_i\alpha/\gamma)} \right) \right] \\ \times I_\nu \left[\left(\frac{2}{\alpha\gamma D} \right) \left(\frac{q^{-\alpha/2} \exp([s+s_i]\alpha/[2\gamma])}{\exp(s\alpha/\gamma) - \exp(s_i\alpha/\gamma)} \right) \right] \quad (\text{B53})$$

$$f(s, q) = \left(\frac{2h_i}{\alpha\gamma D} \right) \frac{q^{-(3+\alpha)/2} \exp([s/\gamma][3+\alpha]/2)}{[\exp(s\alpha/\gamma) - \exp(s_i\alpha/\gamma)]} \\ \times \exp \left[- \left(\frac{1}{\alpha\gamma D} \right) \left(\frac{q^{-\alpha} \exp(s\alpha/\gamma) + \exp(s_i\alpha/\gamma)}{\exp(s\alpha/\gamma) - \exp(s_i\alpha/\gamma)} \right) \right] \\ \times I_\nu \left[\left(\frac{2}{\alpha\gamma D} \right) \left(\frac{q^{-\alpha/2} \exp([s+s_i]\alpha/[2\gamma])}{\exp(s\alpha/\gamma) - \exp(s_i\alpha/\gamma)} \right) \right] \exp(-[s-s_i][1+t_0/\tau_{\text{esc}}]) \quad (\text{B54})$$

By integrating over the initial time for particle injection and taking $s = 0$, we derive the steady-state distribution,

$$f_0(q) = \text{Lim}[s_0 \rightarrow \infty] \frac{1}{s_0} \int_{-s_0}^0 f(s=0, q) \quad (\text{B55})$$

$$= \text{Lim}[s_0 \rightarrow \infty] \left(\frac{2h_0}{\alpha\gamma D} \right) q^{-(3+\alpha)/2} \int_{-s_0}^0 ds_i \frac{1}{[1 - \exp(s_i\alpha/\gamma)]} \\ \times \exp \left[- \left(\frac{1}{\alpha\gamma D} \right) \left(\frac{q^{-\alpha} + \exp(s_i\alpha/\gamma)}{1 - \exp(s_i\alpha/\gamma)} \right) \right] \\ \times I_\nu \left[\left(\frac{2}{\alpha\gamma D} \right) \left(\frac{q^{-\alpha/2} \exp(s_i\alpha/[2\gamma])}{1 - \exp(s_i\alpha/\gamma)} \right) \right] \exp(s_i[1+t_0/\tau_{\text{esc}}]) \quad (\text{B56})$$

where $h_0 = h_i/s_0$. We treat the cases of $\alpha > 0$ and $\alpha < 0$ separately. For $\alpha > 0$, it is convenient to switch to the integration variable,

$$y_i = \exp(s_i\alpha/\gamma) \quad (\text{B57})$$

in which case the steady-state solution becomes

$$f_0(q, \alpha > 0) = \left(\frac{2h_0}{\alpha\gamma D} \right) q^{-(3+\alpha)/2} \int_0^1 \frac{dy_i}{y_i} \frac{1}{\alpha[1-y_i]} \\ \times \exp \left[- \left(\frac{1}{\gamma D} \right) \left(\frac{q^{-\alpha} + y_i}{\alpha(1-y_i)} \right) \right] \\ \times I_\nu \left[\left(\frac{2}{\gamma D} \right) \left(\frac{q^{-\alpha/2} \sqrt{y_i}}{\alpha(1-y_i)} \right) \right] y_i^{[1+t_0/\tau_{\text{esc}}]\gamma/\alpha} \quad (\text{B58})$$

The case with $\alpha < 0$ is similar to equation (B58), but the limits of integration are modified,

$$f_0(q, \alpha < 0) = \left(\frac{2h_0}{|\alpha|\gamma D} \right) q^{-(3+\alpha)/2} \int_1^\infty \frac{dy_i}{y_i} \frac{1}{|\alpha|[y_i-1]} \\ \times \exp \left[- \left(\frac{1}{\gamma D} \right) \left(\frac{q^{-\alpha} + y_i}{|\alpha|(y_i-1)} \right) \right] \\ \times I_\nu \left[\left(\frac{2}{\gamma D} \right) \left(\frac{q^{-\alpha/2} \sqrt{y_i}}{|\alpha|(y_i-1)} \right) \right] y_i^{[1+t_0/\tau_{\text{esc}}]\gamma/\alpha} \quad (\text{B59})$$

The expression is made more tractable by transforming to the integration variable $w_i = 1/y_i$,

$$f_0(q, \alpha < 0) = \left(\frac{2h_0}{|\alpha|\gamma D} \right) q^{-(3+\alpha)/2} \int_0^1 dw_i \frac{1}{|\alpha|[1-w_i]}$$

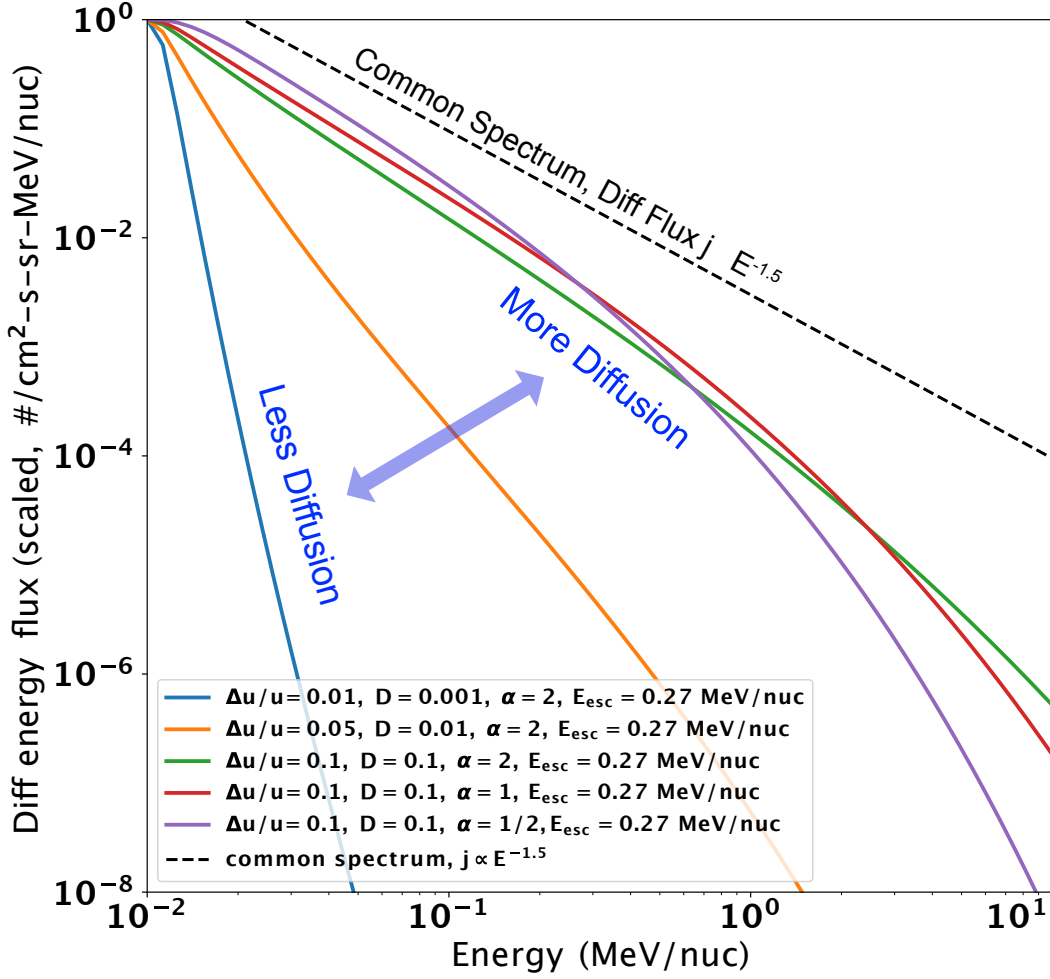


Figure 13. Differential flux (scaled) based on the injection flux. Curves are shown as a function of energy for various levels of diffusive acceleration, momentum diffusion, and the scaling of diffusion with momentum as detailed in the appendix. High levels of diffusion converge to a common spectrum beneath the escape energy with differential energy flux proportional to $E^{-1.5}$. Low levels of diffusion result in a very soft spectrum. The diffusive power-law has a distribution function that scales as $p^{-\gamma}$.

$$\begin{aligned}
 & \times \exp \left[- \left(\frac{1}{\gamma D} \right) \left(\frac{w_i q^{-\alpha} + 1}{|\alpha|(1-w_i)} \right) \right] \\
 & \times I_\nu \left[\left(\frac{2}{\gamma D} \right) \left(\frac{q^{-\alpha/2} \sqrt{w_i}}{|\alpha|(1-w_i)} \right) \right] w_i^{[1+t_0/\tau_{\text{esc}}]\gamma/|\alpha|}
 \end{aligned} \tag{B60}$$

We take, for simplicity and clarity, the escape time inversely proportional to energy such that

$$\frac{t_0}{\tau_{\text{esc}}} = \sqrt{\frac{E}{E_{\text{esc}}}}. \tag{B61}$$

Results are shown in Figure 13 for an array of levels of $\Delta u/u$, D , and α . In each case, we take $E_{\text{esc}} = 0.27$ MeV/nuc. Higher rates of diffusion result in a spectrum close to the common spectrum with differential flux $\propto E^{-1.5}$, as discussed by Fisk & Gloeckler (2008), Hill et al. (2009), and Dayeh et al. (2009).

B.3. *Escape from the acceleration region*

Results of Schwadron et al. (2015) reveal that escape from the acceleration region must be considered when treating the behavior of distribution functions at relatively high energy. Particle escape from an accelerator occurs in a number of different ways. In Schwadron et al. (2015), plasma flows along a shock surface sweep magnetic field lines out of the acceleration region at a steady rate. This form of escape is particularly important at shocks and compressions where the magnetic field is almost perpendicular to the plasma velocity gradient, which acts as the source of particle acceleration.

In other circumstances such as near QSL regions and quasi-parallel shocks or compressions, the magnetic field has a relatively small angle relative to the plasma flow. In this case, the magnetic field remains tied to the acceleration region, and particles escape by leaving the magnetic field line, either through gradient or curvature drift, or through cross-field diffusion. In this case, we consider the acceleration region to have a scale-length L_{\perp} perpendicular to the magnetic field. We treat the effect of perpendicular diffusion, and consider a perpendicular diffusion coefficient given by $\kappa_{\perp} = \eta\kappa_{\parallel}$.

We take, for simplicity, the case of a constant parallel mean free path, $\lambda_{\parallel} = 5 R_{\odot}$ (or 0.023 au) referenced at 1 MeV/nuc in the low corona. Note that this mean free path is similar to values at 1 au. For example, Dröge (2000) find typical scattering mean free paths in the range of 0.02 to 0.5 au observed near 1 au. The radial dependence of the scattering mean free path, particularly for protons, is not widely understood. In the case of relativistic electrons, Kallenrode et al. (1992) found that $> 1 - 10$ MeV electrons observed on Helios show a power-law dependence of the radial mean free path, $\lambda_{\parallel} \propto r^{\beta}$, with β in the range 0 to 0.3. The result is also in line with recent work from the IS \odot IS instruments (McComas et al. 2016) on Parker Solar Probe (Fox et al. 2016). Giacalone et al. (2023) studied a shock observed for 0.05 to 2 MeV protons when the spacecraft was near 0.35 au. Particles far upstream from the shock showed scattering mean free paths in the range 0.02 to 0.1 au ($4 - 21 R_{\odot}$), which is compatible with typical ranges observed at 1 au. It is notable that near the shock, increased levels of turbulence reduce the scattering mean free path by a factor of $\sim 1/10$, which greatly increases the rate of acceleration near the shock. For the ratio of perpendicular to parallel diffusion, we adopt a value of $\eta = 0.01$. This value is intermediate to values found in a number of studies: the range of 0.01 to 0.05 was considered by Giacalone & Jokipii (1999); in contrast, Zank et al. (2006) found a much lower value $\eta \sim 0.001$.

Applying these values, we estimate the escape time $\tau_{\text{esc}} = L_{\perp}^2 / \kappa_{\perp}$. For simplicity, we take a constant perpendicular mean free path, resulting in

$$\tau_{\text{esc}} = t_0 \sqrt{\frac{E_{\text{esc}}}{E}} \quad (\text{B62})$$

where

$$E_{\text{esc}} = (3L/\lambda_{\perp})^2 E_{\text{sw}} \quad (\text{B63})$$

where we have taken $L_{\perp} \sim L$, and $E_{\text{sw}} = mu_{\text{sw}}^2/2$ is the characteristic solar wind energy for a species of mass m . With $\lambda_{\parallel} = 5 R_{\odot}$, $L = 0.3 R_{\odot}$, and $\eta = 0.01$, we find $E_{\text{esc}} = 0.27$ MeV/nuc.

C. CONNECTION WITH RANDOM STOCHASTIC PROCESSES

The treatment of reconnection exhausts results in a simple interpretation for the acceleration mechanism at work, while also suggesting a broader connection to the superposition of stochastic processes (Schwadron et al. 2010a). Notably, the magnetic pump is in the class of superposition solutions, Fisk et al. (2010). This is important here as it connects particle acceleration from stochastic fluctuations in the magnetic field magnitude with the superposition theory.

In §B.1, we found that the diffusive acceleration process proceeds along an acceleration characteristic, with the distribution function varying with an inverse exponential in time for energies below the escape energy (see equation B29). The fixed characteristic for acceleration depends on the presence of a first-order Fermi process. In contrast, the interchange reconnection exhausts create variations in both strength of the magnetic field and in the density that result in second-order Fermi acceleration (see equation A10). The acceleration in this case does not proceed strictly along acceleration characteristics. Instead, there is an array of characteristics that are populated as energy diffusion broadens the energy distribution as a function of time. Fundamentally, the dependence on an inverse exponential in

time remains (B34). But the final solution becomes much more complex since many different inverse exponential terms contribute, depending on the relative time of particle injection and the broadening through energy diffusion.

The presence of inverse exponential time-dependence suggests a deeper connection with stochastic processes. The example of waiting time distributions provides perhaps a simplified way to understand this connection.

Suppose there is a series of events separated by waiting time t . These events may be of any sort provided that they are randomly distributed. For example, previous treatments of waiting time distributions have been applied to solar flares (Wheatland 2000), (Dragulescu & Yakovenko 2000) (Yakovenko & Rosser, Jr. 2009). A given inverse exponential distribution of waiting times has a mean event rate β . The probability of an event with a given waiting time is therefore,

$$P_\tau(t) = \beta \exp(-\beta t). \quad (\text{C64})$$

We can take the first moment of this probability distribution to determine the average waiting time,

$$\tau = \int_0^\infty t P(t) dt = 1/\beta. \quad (\text{C65})$$

The average waiting time is simply the inverse of the mean event rate. This formulation is adequate provided that there is only one process proceeding with a specific mean event rate.

Wheatland (2000) developed the more general case when there is an ensemble of processes each with a distinct occurrence rate. The processes are treated as states, and have random or Poisson behavior if the states maximize the entropy associated with these states. Applying this entropy constraint to ensure the states are randomly distributed results in a waiting time distribution that conforms to a kappa distribution.

These same considerations applied to waiting time distributions also apply to the distribution functions of energetic particles (Schwadron et al. 2010a). The fact that the waiting time distribution for a given process depends on the inverse of an exponential in time aligns precisely with behavior of a given acceleration process, as found previously (see equations B34 and B34).

The waiting time has a deeper connection to stochastic processes when considering the spatial distribution of particles from accelerated sources. Consider a characteristic distance L_s from a source defined such that $L_s = v/\beta$. With this definition, the waiting time distribution is expressed

$$P_\tau(t) = (v/L_s) \exp(-vt/L_s). \quad (\text{C66})$$

The average waiting time is now $\tau = L_s/v$ and represents the characteristic propagation time from the source. Small waiting times $t < L_s/v$ are more likely because particles build-up near the source and are separated over distance $\ell_s < L_s$. Larger waiting times $t > L_s/v$ are less likely since they characterize particles with separations $\ell_s > L_s$ larger than the distance to the source.

We arrive at a similar form for the waiting time distribution by accounting for particle acceleration. In the presence of acceleration, particle speeds increase with time. Shorter distances between particles indicates short waiting times, a location nearer the source, and smaller amounts of acceleration. Particles propagating further from the source are capable of experiencing larger amounts of acceleration.

The accelerator could be the presence of small-scale fluctuations of the magnetic field magnitude and associated transit-time damping. For example, particles can cross field lines and gain energy from the $\mathbf{u} \times \mathbf{B}$ field. In this example, the acceleration is applied over the waiting time, and the speed increases as $v = c_b + at$, where a is the average acceleration over time t , and c_b represents the characteristic speed for the bulk of the distribution. Larger waiting times are associated with a minority of particles capable of accessing larger amounts of acceleration. The waiting time distribution is expressed as

$$P_\tau(v) = \beta \exp(-\beta[v - c_b]/a). \quad (\text{C67})$$

The break in the distribution occurs at a characteristic speed $v = a/\beta$. The speed distribution, $P_u(v)$, follows,

$$\begin{aligned} P_u(v) &\propto (1/[dv/dt])P_\tau(v) \\ &= C_n(\beta/a) \exp(\beta c_b/a) \exp(-\beta v/a) \\ &= \beta/a \exp(-\beta v/a) \end{aligned} \quad (\text{C68})$$

The normalization constant C_n is determined by the definition of a probability distribution, $\int_0^\infty dv P_u = 1$, while the mean speed of the distribution is given by $u = a/\beta$.

Schwadron et al. (2010a) considered the waiting time distribution as a random or Poisson process. The almost equal probability of waiting times below the break at $t < 1/\beta$ qualifies the Poisson process as random. In an acceleration process, it also takes some time to achieve a given particle speed v . The acceleration time behaves effectively as the waiting time.

Each process is associated with a probability distribution and a mean speed u tied to the process rate. An array of these processes is considered as an array of states in a system with a given mean inverse speed ζ_0 . Since the acceleration processes are random, the distribution of states is subject to the maximization of the Boltzmann entropy, given the constraint of specific average inverse speed (Schwadron et al. 2010a). Therefore, the state distribution is given by,

$$F(\zeta) = \exp[-\zeta/\zeta_0]/\zeta_0. \quad (\text{C69})$$

Schwadron et al. (2010a) demonstrated that the superposition of these states results in a kappa-distribution. The superposed probability distribution is

$$P_s(v) = 2\zeta_0/(v\zeta_0 + 1)^3 \quad (\text{C70})$$

and the associated particle distribution is

$$\begin{aligned} f(v > c_s) &= nP_s(v)/(4\pi v^2) \\ &= \left(\frac{n}{2\pi v^2}\right) \frac{\zeta_0}{(v\zeta_0 + 1)^3} \end{aligned} \quad (\text{C71})$$

where n is the density of the distribution, and the distribution function is explicitly considered for particle speeds greater than the the core or thermal speed of the distribution, $v > c_s$.

An interesting and important result that follows from this distribution is the v^{-5} distribution at high particle speeds. We note that this distribution is similar to that found in §B.2 in the limit of strong diffusion. While there is no one acceleration rate at all energies, there is a rate of diffusion in momentum space, which controls the rate of acceleration. Over short periods of time compared to the total acceleration time, the change in speed varies approximately linearly with time. The tail of the accelerated population reveals the superposition of states in the distribution. The superposition of exponential states of particle speed is inevitable (see equation C68) provided that particles are not subject to rapid acceleration by a specific first-order mechanism, or that states are not overtaken, as occurs in shocks, or in non-linear cases when the acceleration decreases with particle speed. In such exceptions, the buildup of states collapses to a specific velocity and behaves in a manner similar to a soliton solution.

The diffusive process provides a build-up in particle speed for the distribution through multiple encounters of fluctuations in the magnetic field magnitude and the density of the plasma. Each of these fluctuations behaves as an individual state with a specific acceleration and approximately exponential dependence on particle speed. Since diffusion is inherently random, the entropy of states must be maximized. Therefore, in the limit of strong diffusion, the superposed distribution must follow the kappa function (C71).

The agreement between the kappa function and the more detailed analytic treatment in §B.2 is not accidental. However, the diffusive and first-order processes dealt with previously require an injection speed where particles are capable of moving upstream in the plasma. The superposition of states does not require an injection speed. The difference is that acceleration acts in the frame of the solar wind, and operates as a continuum of stochastic processes or states. This occurs provided that there is a turbulent cascade from the sites of reconnection that drive the fluctuations in the plasma.

The main parameters that enter the estimation of the stochastic distribution is the density and the mean inverse speed ζ_0 . Near the QSL particles gain energy through stochastic momentum diffusion. It is mesoscale and small-scale structures in the solar wind that provide acceleration. The source of energy for these structures is reconnection within the QSL. The QSL structures cascade down in size as they interact with the surrounding solar wind, driving energy from larger to smaller scales. The rate of momentum diffusion D_{pp}^ℓ in these smaller structures is derived based on their sizescale ℓ and the sizescale L of larger region near the QSL,

$$D_{pp}^\ell = \frac{\ell}{L} D_{pp}. \quad (\text{C72})$$

The mean inverse speed is tied to acceleration in the mesoscale and small-scale structures,

$$\frac{1}{\zeta_0} = \sqrt{\frac{D_{pp}^\ell(c_s) \ell}{m^2 c_s}} \quad (\text{C73})$$

where the momentum diffusion rate $D_{pp}^\ell(c_s)$ is evaluated at the sound speed c_s .